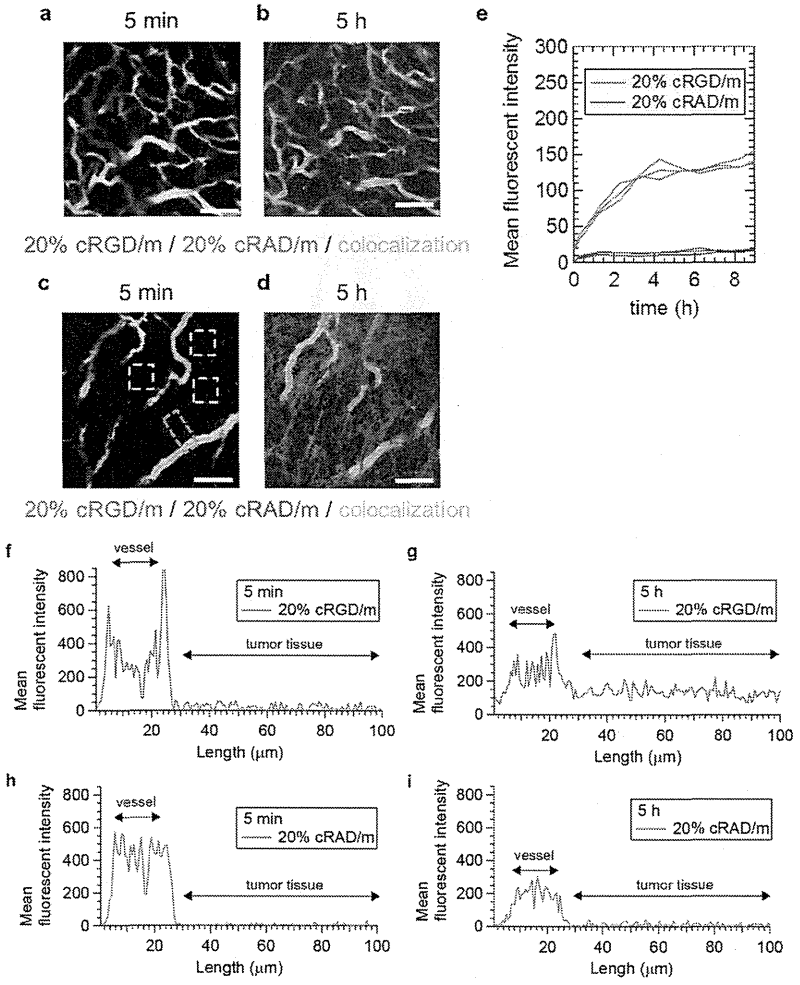

Figure 6. IVCLSM of DACHPt/m. IVCLSM observations of 20% cRAD/m (green) and 20% cRGD/m (red) in blood vessels and tumors at (a) 5 min and (b) 5 h after intravenous coadministration. IVCLSM observations of 20% cRAD/m (red) and 20% cRGD/m (green) in blood vessels and tumors at (c) 5 min and (d) 5 h after intravenous coadministration. Their colocalization is shown in yellow. The spectral images were unmixed to determine the Alexa 647 (red), Dylight 488 (green), and autofluorescence levels. Scale bars represent 100 μm in all images. (e) Quantitative analysis of the amounts of micelles in tumor sites based on the IVCLSM results. Fluorescence profiles of cRGD/m (green) and cRAD/m (red) in the region selected (indicated by a white rectangle in part c). (d) Permeation profiles of 20% cRGD/m (green) and 20% cRAD/m (red) from the blood vessels to the tumors in the selected region (indicated by a blue rectangle in part c) at 5 min (f and h) and at 5 h (g and i).

fluorescence signal of cRGD/m along the lining of the tumor vessel was confirmed 5 min after administration. Then, the intensity values of green fluorescence (cRGD/m) at the tumor tissue increased from 0 to approximately 150 during the initial 5 h (Figure 6g). On the other hand, the cRAD/m (red) was unable to penetrate tumor vasculature (Figure 6h and i). We confirmed that subcutaneous glioblastoma models showed the expression of "tight junctions" (Claudin 5-positive) and "pericytes" (αSMA-positive) (Supporting Information Figure S3) by immunohistochemical analysis,[46−48] indicating the existence of the vascular/tumor barriers. Hence, we proved that this differential permeability is attributed to the potential of cRGD ligands on the micelles to induce integrin-mediated active transport specifically through the vascular barrier. Overall, it is reasonable to conclude that the cRGD/m can enter the tumor sites *via* active transport-mediated pathways, most likely transcytosis as the vesicular transport is enhanced in the vasculature of brain tumor.[49,50] Although the integrin targeting by using cRGD has been considerably investigated, the direct visual evidence to support active transport across the vascular barrier of glioblastoma is reported for the first time in this study as far as we know.

Further research into the antitumor efficacy by utilizing orthotopic brain tumor models would clarify the availability of cRGD/m in clinical settings. We implanted U87MG-Luc2 cancer cells into the brains of BALB/c nude mice (Supporting Information) and monitored the tumor growth inhibition effect by luciferase imaging. Five days after tumor inoculation, 20% cRGD/m and 20% cRAD/m were administered iv at a dose of 4 mg/kg on a DACHPt basis every other day (total of three injections). Oxaliplatin (dose = 8 mg/kg) was also used as a control-free drug with the same dosing schedule. The IVIS images showed that the signals from

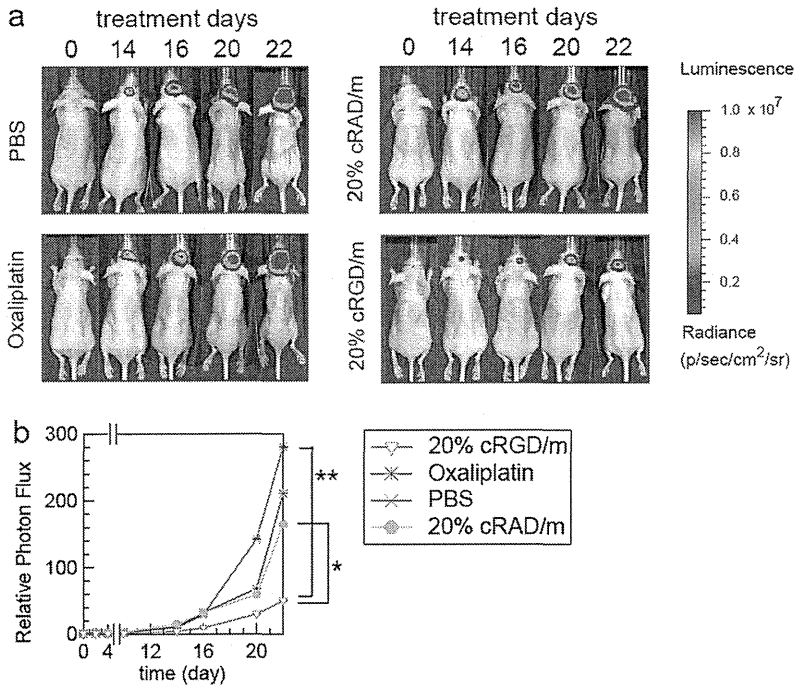

Figure 7. Effects of cRGD-linked DACHPt/m in orthotopic U87MG glioblastoma. The mice were anesthetized with isoflurane and injected intravenously with 150 mg/kg luciferin. At 1−2 min after luciferin injection, the mice were imaged for 1−60 s. (a) Representative *in vivo* bioluminescence images of the mice from PBS-, oxaliplatin-, 20% cRAD/m-, and 20% cRGD/m-treated groups. The colored scale bar indicates the intensity of bioluminescence in p/s/cm^2/sr. (b) Comparison of tumor growth inhibition with 20% cRGD/m and 20% cRAD/m. Five days after tumor cell transplantation, the mice were injected intravenously with micelles. The micelles (4 mg/kg based on DACHPt) were administered every other day (three injections). Oxaliplatin was used as a control platinum drug (dose = 8 mg/kg) with the same treatment schedule. Data represent mean ± SEM (n = 12). Two-way ANOVA was used to analyze differences in the tumor mass volume, and $^{**}p < 0.001$ and $^{*}p < 0.01$ were considered significant.

the cRGD/m-administrated group were clearly weaker than other groups (Figure 7a). On the basis of the quantification of the bioluminescent data from the head area on day 22, approximately 5-fold lower photon flux was observed in the mice treated with 20% cRGD/m compared to those treated with oxaliplatin and 20% cRAD/m (Figure 7b). These results indicate that cRGD is a key to deliver the PM into orthotopic brain tumor models. Altogether, we found that linkage of the ligand molecule cRGD to PMs allows active transport-mediated penetration into tumor tissue beyond BBTB in brain tumor models, achieving potent antitumor activity.

CONCLUSION

In this study, we designed and synthesized a series of DACHPt/m with different percentages of cRGD ligand for the treatment of brain tumors. The constructs and their properties were fully characterized and subjected to *in vitro* and *in vivo* studies, including cytotoxicity assays, cellular uptake analyses, and evaluations of therapeutic efficacy in tumor-bearing mice. Consequently, 20% cRGD/m exhibited significantly higher growth inhibitory effect against GBM tumors compared to the nontargetable 20% cRAD/m. Furthermore, the IVCLSM results demonstrated the tumor-accumulation characteristics of cRGD/m, which prompted the identification of the active transport of cRGD-mediated drug delivery across vascular and tumor barriers, *i.e.*, BBTB. These findings indicate that cRGD-mediated DDS is a powerful strategy for targeting therapy of glioblastoma through the facilitated drug delivery beyond the BBTB.

MATERIALS AND METHODS

Materials, Cell Lines, and Animals. Information regarding materials, cell line (human glioblastoma cell line (U87MG)), and animals (BALB/c nude mice; Oriental Yeast Co., Ltd., Tokyo, Japan) is described in the Supporting Information. All animal experiments were performed in accordance with the Guidelines for the Care and Use of Laboratory Animals as stated by the University of Tokyo.

Preparation of Polymers and PMs. Poly(ethylene glycol)-*b*-poly(L-glutamic acid) (MeO-PEG-*b*-P(Glu)) and maleimide-conjugated poly(ethylene glycol)-*b*-poly(L-glutamic acid) (Mal-PEG-*b*-P(Glu)) were designed and synthesized based on our developed methods.[35,39,40] MeO-PEG-*b*-P(Glu) was fluorescently labeled by conjugating the Dylight 488, Alexa 555, and Alexa 647 succinimidyl esters to the ω-amino groups of polymers. The polymers were characterized by ^{1}H NMR measurement (solvent: $CDCl_3$, D_2O, and *d*-DMSO; temperature: 25 °C), size exclusion chromatography in DMF containing lithium bromide (10 mM) or in 10 mM PBS containing 150 mM NaCl, and high-performance liquid chromatography in 2 mM PB (pH = 6.5). Details of the procedures used for

polymer synthesis and characterization are described in the Supporting Information. DACHPt/m, cRGD/m, and cRAD/m were prepared according to a method described previously, with a slight modification. In brief, the typical procedure used for the preparation of 20% cRGD/m was as follows: a mixture of DACHPt-(NO_3)Cl, MeO-PEG-*b*-P(Glu), and Mal-PEG-*b*-P(Glu) ([Glu] = 5 mmol/L, [DACHPt]/[Glu] = 1.0 (mol/mol), and [MeO-PEG-*b*-P(Glu)]/[Mal-PEG-*b*-P(Glu)] = 1.0/1.0 (mol/mol)) was stirred at 37 °C for 120 h. The reaction mixture was transferred to a cellophane tube (Spectra/Pro 6 membrane: MWCO, 3500) and dialyzed for 1 day against distilled water, followed by ultrafiltration (MWCO, 30 000) to yield the maleimide-functionalized DACHPt/m. Next, cyclo[RGDfK(CX-)] (cRGD peptide, X = ε-Acp) was added to the maleimide-functionalized DACHP/m solution and incubated at rt. After 18 h, the micelle solution was purified by ultrafiltration (MWCO, 100 000) to give the 20% cRGD-linked DACHPt/m (20% cRGD/m). The number of cRGD linked was estimated by ^{1}H NMR measurement (solvent, D_2O; temperature, 25 °C). The control DACHPt/m (ctrl/m), 5% and 40% cRGD-linked (5% cRGD/m and 40% cRGD/m), and 20% cRAD-linked (20% cRAD/m) DACHPt/m were prepared in the same manner as described above, with the slight exception that the molar ratios of [MeO-PEG-*b*-P(Glu)/Mal-PEG-*b*-P(Glu)] were changed from 50/50 to 100/0 for ctrl/m, 10/90 for 5% cRGD/m, and 0/100 for 40% cRGD/m. The size distribution of DACHPt/m was evaluated by DLS measurements at 25 °C, and the zeta potentials of the micelles were measured in phosphate buffer at pH 7.4 using a Zetasizer Nano ZS90 (Malvern Instruments). The platinum content of the micelles was determined by ICP-MS using a Hewlett-Packard HP 4500 ICP-MS system. More detailed information is provided in the Supporting Information.

Cellular Uptake of the Platinum Drug. U87MG cells (2×10^7) were seeded into a 225 cm^2 cell culture flask. After 12 h incubation, the medium was replaced with fresh medium (30 mL), which included 10 μM (on a platinum basis) oxaliplatin or micelles. Then, cells were incubated for 1, 3, 8, and 24 h. The cells were then washed three times with PBS, scraped, and harvested. The cells were resuspended in 1000 μL of water and freeze-dried to yield the dried samples. Acid digestion of all samples was carried out with *ca.* 1.0 mL of concentrated HNO_3 at 200 °C, and then the dried samples were dissolved in 1 vol % HNO_3(aq) (1.0 mL). Platinum concentration was measured by ICP-MS. All experiments were repeated four times, and the average platinum content (μg)/2×10^7 cells was calculated.

***In Vitro* Cytotoxicity Assay.** The 50% growth inhibitory concentrations (IC_{50}) of free oxaliplatin, ctrl/m, the 5%, 20%, and 40% cRGD/m, and 20% cRAD/m were evaluated in U87MG cells using the Cell Counting Kit-8 (Dojindo Laboratories). The cells (2000 cells/50 μL) were cultured in DMEM containing 10% FBS in a 96-well multiplate. The cells were then exposed to oxaliplatin or the micelles for 48 h. The manufacturer's reagent (10 μL) was added, and then the cells were incubated for 2 h. The absorbance of media was measured at 450 nm using a microplate reader (Biorad). The inhibitory effect after short-term drug exposure was tested in the same manner as described above, with the following slight difference: different concentrations of oxaliplatin solution or micelle solution were added to the 96-well multiplate, and the cells were incubated for 3 h. The medium was replaced with fresh medium (100 μL) and incubated for 48 h. The experiments were repeated three times, and the average IC_{50} values were calculated.

Antitumor Activity Assay. In order to evaluate the antitumor efficacy of DACHPt/m using different molarities of ligand molecules, subcutaneous tumor models in BALB/c nude mice (Oriental Yeast Co., Ltd., Tokyo, Japan) (n = 6) were treated three times intravenously every other day with 4 mg/kg (on a DACHPt basis) of 20% cRGD/m and 20% cRAD/m. The antitumor activities were evaluated by measuring the tumor size (V), which was estimated using the following equation: $V = ab^2/2$, where a and b are the major and minor axes of the tumor measured using a Vernier microcaliper. In the antitumor activity assay using orthotopic tumor models, BALB/c nude mice (n = 12) were treated three times intravenously every other days with 4 mg/kg (on a DACHPt basis) of 20% cRGD/m and 20% cRAD/m. *In vivo* imaging was performed using an IVIS Spectrum (Xenogen Corporation). Luciferin (Promega) was used as a substrate for luciferase. The mice were anesthetized with isoflurane (Mylan Inc.) and injected intravenously with 150 mg/kg luciferin. At 1–2 min after luciferin injection, the mice were imaged for 1–60 s. The regions of interest (ROIs) were selected to measure the tumor volume and background. The photons emitted from ROIs were quantified using Living Image software (ver. 4.1). *In vivo* luciferase activity was expressed as photons/s/cm^2/sr. Two-way analysis of variance (ANOVA) was used to analyze the differences in the tumor mass volume between the experimental and control groups. Data analysis was performed using GraphPad Prism version 5.04 for Windows (GraphPad Software). $^{**}p < 0.001$ was considered statistically significant in each analysis.

Plasma Clearance and Tumor Accumulation of DACHPt/m. To evaluate the plasma clearance and tumor accumulation of DACHPt/m *in vivo*, BALB/c nude mice bearing U87MG tumors (n = 6) were intravenously injected with 20% cRGD/m, 20% cRAD/m, and oxaliplatin at 100 mg/mouse on a DACHPt basis. The mice were sacrificed 1, 4, 8, and 24 h after injection. The tumors were excised, washed with PBS, and weighed after removing excess fluid. Blood was collected from the inferior vena cava, heparinized, and centrifuged to obtain the plasma. Acid digestion of all samples was carried out using *ca.* 1.0 mL of concentrated HNO_3 at 200 °C, and the dried samples were dissolved in 1 vol % HNO_3(aq) (1.0 mL). Platinum concentration was measured by ICP-MS.

IVCLSM. IVCLSM was performed using a Nikon A1R confocal laser scanning microscope system attached to an upright ECLIPSE FN1 machine, which was equipped with a Plan Apo VC 20× DIC N2 (numerical aperture: 0.75) objective lens (Nikon), as described in our previous report.[37] All pictures/movies were acquired as spectral images using 10 μm of confocal slices. Video images of the tumors were aquired at 5 min intervals for 15 min. Video acquisition was continued at 1 h intervals. Two-hundred microliters of solution containing Dylight 488- and Alexa 647-labeled micelles was administered *via* a tail vein catheter. The AFU value of each micelle solution was adjusted to *ca.* 6000 measured by NanoDrop. Video acquisition was initiated 280 s after administration. Dylight 488 and Alexa 647 were excited using lasers at wavelengths of 488 and 638 nm, respectively. Acquired data were processed using Nikon NIS Elements (ver. 4.00.06). The spectral images were unmixed with respect to Dylight 488, Alexa 647, and autofluorescence. ROIs were selected manually using Nikon NIS Elements (ver. 4.00.06).

Conflict of Interest: The authors declare no competing financial interest.

Acknowledgment. We thank C. Sakamoto, R. Shiratori, and N. Henzan for the synthesis of polymers, and S. Ogura and A. Miyoshi for help with animal experiments. This work was supported by the Funding Program for World-Leading Innovative R&D on Science and Technology (FIRST Program) from the Japan Society for the Promotion of Science (JSPS) and Grants-in-Aid for Scientific Research from the Japanese Ministry of Health, Labour and Welfare (MHLW). It was partially supported by Grants-in-Aid for Young Scientists (A), Challenging Exploratory Research, and JSPS Fellows.

Supporting Information Available: Details of the materials, measurement techniques, synthesis of polymers, micelle preparation, information on the biological experiments related to the knockdown of intregrin alpha V, real-time PCR, detection of integrin receptors, and animal preparation, and IVCLSM video. This material is available free of charge *via* the Internet at http://pubs.acs.org.

REFERENCES AND NOTES

1. Rat, J. S. Molecular Mechanisms of Glioma Invasiveness: The Role of Proteases. *Nat. Rev. Cancer* **2003**, *3*, 489–501.
2. Arko, L.; Katsyv, I.; Park, G. E.; Luan, W. P.; Park, J. K. Experimental Approaches for the Treatment of Malignant Gliomas. *Pharmacol. Ther.* **2010**, *128*, 1–36.
3. Mangiola, A.; Anile, C.; Pompucci, A.; Capone, G.; Rigante, L.; De Bonis, P. Glioblastoma Therapy: Going Beyond Hercules Columns. *Expert Rev. Neurother.* **2010**, *10*, 507–514.

4. Jain, R. K.; Tomaso, di E.; Duda, D. G.; Loeffler, J. S.; Sorensen, A. G.; Batchelor, T. T. Angiogenesis in Brain Tumours. *Nat. Rev. Neurosci.* **2008**, *8*, 610–622.
5. Wen, P. Y.; Kesari, S. Malignant Gliomas in Adults. *N. Engl. J. Med.* **2008**, *359*, 492–507.
6. Avgeropoulos, N. G.; Batchelor, T. T. New Treatment Strategies for Malignant Gliomas. *Oncologist* **1999**, *4*, 209–224.
7. Jones, T. S.; Holland, E. C. Standard of Care Therapy for Malignant Glioma and Its Effect on Tumor and Stromal Cells. *Oncogene* **2012**, *31*, 1995–2006.
8. Rich, J. N.; Bigner, D. D. Development of Novel Targeted Therapies in the Treatment of Malignant Glioma. *Nat. Rev. Drug Discovery* **2004**, *3*, 430–446.
9. Reardon, D. A.; Perry, J. R.; Brandes, A. A.; Jalali, R.; Wick, W. Advances in Malignant Glioma Drug Discovery. *Expert Opin. Drug Discovery* **2011**, *6*, 739–753.
10. Groothuis, D. R. The Blood-Brain and Blood-Tumor Barriers: A Review of Strategies for Increasing Drug Delivery. *Neuro-Oncology* **2000**, *2*, 45–59.
11. Ningaraj, N. S. Drug Delivery to Brain Tumours: Challenges and Progress. *Expert Opin. Drug Delivery* **2006**, *3*, 499–509.
12. Sarin, H. Recent Progress towards Development of Effective Systemic Chemotherapy for the Treatment of Malignant Brain Tumors. *J. Transl. Med.* **2009**, *7*, 77.
13. He, H.; Li, Y.; Jia, X. R.; Du, J.; Ying, X.; Lu, W. L.; Lou, J. N.; Wei, Y. PEGylated Poly(amidoamine) Dendrimer-Based Dual-Targeting Carrier for Treating Brain Tumors. *Biomaterials* **2011**, *32*, 478–487.
14. Xin, H.; Jiang, X.; Gu, J.; Sha, X.; Chen, L.; Law, K.; Chen, Y.; Wang, X.; Jiang, Y.; Fang, X. Angiopep-Conjugated Poly-(ethylene glycol)-co-Poly(ε-caprolactone) Nanoparticles as Dual-Targeting Drug Delivery System for Brain Glioma. *Biomaterials* **2011**, *32*, 4293–4305.
15. Pardridge, W. M. Drug and Gene Delivery to the Brain: The Vascular Route. *Neuron* **2002**, *36*, 555–558.
16. Muldoon, L. L.; Soussain, C.; Jahnke, K.; Johanson, C.; Siegal, T.; Smith, Q. R.; Hall, W. A.; Hynynen, K.; Senter, P. D.; Peereboom, D. M.; *et al.* Chemotherapy Delivery Issues in Central Nervous System Malignancy: A Reality Check. *J. Clin. Oncol.* **2007**, *25*, 2295–2305.
17. Liu, Y.; Lu, W. Recent Advances in Brain Tumor-Targeted Nano-Drug Delivery Systems. *Expert Opin. Drug Delivery* **2012**, *9*, 671–686.
18. Chen, C.; Xu, T.; Lu, Y.; Chen, J.; Wu, S. The Efficacy of Temozolomide for Recurrent Glioblastoma Multiforme. *Eur. J. Neurol.* **2013**, *20*, 223–230.
19. Duncan, R. The Dawning Era of Polymer Therapeutics. *Nat. Rev. Drug Discovery* **2003**, *2*, 347–360.
20. Ferrari, M. Cancer Nanotechnology: Opportunities and Challenges. *Nat. Rev. Cancer* **2005**, *5*, 161–171.
21. Torchilin, V. P. Recent Advances with Liposomes as Pharmaceutical Carriers. *Nat. Rev. Drug Discovery* **2005**, *4*, 145–160.
22. Davis, M. E.; Chen, Z.; Shin, D. Nanoparticle Therapeutics: An Emerging Treatment Modality for Cancer. *Nat. Rev. Drug Discovery* **2008**, *7*, 771–782.
23. Kataoka, K.; Harada, A.; Nagasaki, Y. Block Copolymer Micelles for Drug Delivery: Design, Characterization and Biological Significance. *Adv. Drug Delivery Rev.* **2001**, *47*, 113–131.
24. Nishiyama, N.; Kataoka, K. Current State, Achievements, and Future Prospects of Polymeric Micelles as Nanocarriers for Drug and Gene Delivery. *Pharmacol. Ther.* **2006**, *112*, 630–648.
25. Danhier, F.; Breton, A. L.; Préat, V. RGD-Based Strategies to Target Alpha(v) Beta(3) Integrin in Cancer Therapy and Diagnosis. *Mol. Pharmaceutics* **2012**, *9*, 2961–2973.
26. Matsumura, Y.; Maeda, H. A New Concept for Macromolecular Therapeutics in Cancer Chemotherapy: Mechanism of Tumouritropic Accumulation of Proteins and the Antitumour Agent SMANCS. *Cancer Res.* **1986**, *46*, 6387–6392.
27. Hobbs, S. K.; Monsky, W. L.; Yuan, F.; Roberts, W. G.; Griffith, L.; Torchilin, V. P.; Jain, R. K. Regulation of Transport Pathways in Tumor Vessels: Role of Tumor Type and Microenvironment. *Proc. Natl. Acad. Sci. U.S.A.* **1998**, *95*, 4607–4612.
28. Hynes, R. O. A Reevaluation of Integrins as Regulators of Angiogenesis. *Nat. Med.* **2001**, *8*, 918–912.
29. Hood, J. D.; Cheresh, D. A. Role of Integrins in Cell Invasion and Migration. *Nat. Rev. Cancer* **2002**, *2*, 91–100.
30. Desgrosellier, J. S.; Cheresh, D. A. Integrins in Cancer: Biological Implications and Therapeutic Opportunities. *Nat. Rev. Cancer* **2010**, *10*, 9–22.
31. Taga, T.; Suzuki, A.; Gonzalez-Gomez, I.; Gilles, F. H.; Stins, M.; Shimada, H.; Barsky, L.; Weinberg, K. I.; Laug, W. E. αv-Integrin Antagonist EMD 121974 Induces Apoptosis in Brain Tumor Cells Growing on Vitronectin and Tenascin. *Int. J. Cancer* **2002**, *98*, 690–697.
32. Sheldrake, H. M.; Patterson, L. H. Function and Antagonism of Beta3 Integrins in the Development of Cancer Therapy. *Curr. Cancer Drug Targets* **2009**, *9*, 519–540.
33. Zhan, C.; Gu, B.; Xie, C.; Li, J.; Liu, Y.; Lu, W. Cyclic RGD Conjugated Poly(ethylene glycol)-co-Poly(lactic acid) Micelle Enhances Paclitaxel Anti-Glioblastoma Effect. *J. Controlled Release* **2010**, *143*, 136–142.
34. Zhan, C.; Wei, X.; Qian, J.; Feng, L.; Zhu, J.; Lu, W. Co-Delivery of TRAIL Gene Enhances the Anti-Glioblastoma Effect of Paclitaxel *in Vitro* and *in Vivo*. *J. Controlled Release* **2012**, *160*, 630–636.
35. Cabral, H.; Matsumoto, Y.; Mizuno, K.; Chen, Q.; Murakami, M.; Kimura, M.; Terada, Y.; Kano, M. R.; Miyazono, K.; Uesaka, M.; *et al.* Accumulation of Sub-100 nm Polymeric Micelles in Poorly Permeable Tumours Depends on Size. *Nat. Nanotechnol.* **2011**, *6*, 815–823.
36. Murakami, M.; Cabral, H.; Matsumoto, Y.; Wu, S.; Kano, M. R.; Yamori, T.; Nishiyama, N.; Kataoka, K. Improving Drug Potency and Efficacy by Nanocarrier-Mediated Subcellular Targeting. *Sci. Transl. Med.* **2011**, *3*, 64ra2.
37. Matsumoto, Y.; Nomoto, T.; Cabral, H.; Matsumoto, Y.; Watanabe, S.; Christie, R. J.; Miyata, K.; Oba, M.; Ogura, T.; Yamasaki, Y.; *et al.* Direct and Instantaneous Observation of Intravenously Injected Substances using Intravital Confocal Micro-Videography. *Biomed. Opt. Express* **2010**, *1*, 1209–1216.
38. Nomoto, T.; Matsumoto, Y.; Miyata, K.; Oba, M.; Fukushima, S.; Nishiyama, N.; Yamasoba, T.; Kataoka, K. *In Situ* Quantitative Monitoring of Polyplexes and Polyplex Micelles in the Blood Circulation Using Intravital Real-Time Confocal Laser Scanning Microscopy. *J. Controlled Release* **2011**, *151*, 104–109.
39. Cabral, H.; Nishiyama, N.; Okazaki, S.; Kato, Y.; Kataoka, K. Preparation and Biological Properties of Dichloro(1,2-diaminocyclohexane)platinum(II) (DACHPt)-Loaded Polymeric Micelles. *J. Controlled Release* **2005**, *101*, 223–232.
40. Cabral, H.; Nishiyama, N.; Kataoka, K. Optimization of (1,2-Diaminocyclohexane)platinum(II)-Loaded Polymeric Micelles Directed to Improved Tumour Targeting and Enhanced Antitumour Activity. *J. Controlled Release* **2007**, *121*, 146–155.
41. Yamada, S.; Bu, X. Y.; Khankaldyyan, V.; Gonzales-Gomez, I.; McComb, J. G.; Laug, W. E. Effect of the Angiogenesis Inhibitor Cilengitide (EMD 121974) on Glioblastoma Growth in Nude Mice. *Neurosurgery* **2006**, *59*, 1304–1312.
42. Carter, A. Integrins as Target: First Phase III Trial Launches, But Questions Remain. *J. Natl. Cancer Inst.* **2010**, *102*, 675–677.
43. Fink, K.; Mikkelsen, T.; Nabors, L. B.; Ravin, P.; Plotkin, S. R.; Schiff, D.; Hicking, C.; Picard, M.; Reardon, D. A. Long-Term Effects of Cilengitide, a Novel Integrin Inhibitor, in Recurrent Glioblastoma: A Randomized Phase IIa Study. *J. Clin. Oncol.* **2010**, *28*, 182s.
44. Mikkelsen, T.; Brodie, C.; Finniss, S.; Berens, M. E.; Rennert, J. L.; Nelson, K.; Lemke, N.; Brown, S. L.; Hahn, D.; Neuteboom, B.; *et al.* Radiation Sensitization of Glioblastoma by Cilengitide Has Unanticipated Schedule-Dependency. *Int. J. Cancer* **2009**, *124*, 2719–2727.
45. Nabors, L. B.; Mikkelsen, T.; Rosenfeld, S. S.; Hochberg, F.; Akella, N. S.; Fisher, J. D.; Cloud, G. A.; Zhang, Y.; Carson, K.; Wittemer, S. M.; *et al.* Phase I and Correlative Biology Study of Cilengitide in Patients with Recurrent Malignant Glioma. *J. Clin. Oncol.* **2007**, *25*, 1651–1657.

46. Morita, K.; Sasaki, H.; Furuse, K.; Furuse, M.; Tsukita, S.; Miyachi, Y. Expression of Claudin-5 in Dermal Vascular Endothelia. *Exp. Dermatol.* **2003**, *12*, 289–295.
47. Cooper, I.; Cohen-Kashi-Malina, K.; Teichberq, V. I. Claudin-5 Expression in *in Vitro* Models of the Blood-Brain Barrier. *Methods Mol. Biol.* **2011**, *762*, 347–354.
48. Jiao, H.; Wang, Z.; Liu, Y.; Wang, P.; Xue, Y. Specific Role of Tight Junction Proteins Claudin-5, Occludin, and ZO-1 of the Blood-Brain Barrier in a Focal Cerebral Ischemic Insult. *J. Mol. Neurosci.* **2011**, *44*, 130–139.
49. Stewart, P. A.; Hayakawa, K.; Farrell, C. L.; Del Maestro, R. F. Quantitative Study of Microvessel Ultrastructure in Human Peritumoral Brain Tissue. Evidence for a Blood-Brain Barrier Defect. *J. Neurosurg.* **1987**, *67*, 697–705.
50. Stewart, P. A. Endothelial Vesicles in the Blood-Brain Barrier: Are They Related to Permeability? *Cell. Mol. Neurobiol.* **2000**, *20*, 149–163.

siRNA Conjugates

DOI: 10.1002/anie.201300178

Acidic pH-Responsive siRNA Conjugate for Reversible Carrier Stability and Accelerated Endosomal Escape with Reduced IFNα-Associated Immune Response**

Hiroyasu Takemoto, Kanjiro Miyata, Shota Hattori, Takehiko Ishii, Tomoya Suma, Satoshi Uchida, Nobuhiro Nishiyama, and Kazunori Kataoka**

Small interfering RNA (siRNA) has garnered much interest as a potential drug because of its strong gene-silencing activity.[1] Toward the success in siRNA therapeutics, many strategies have been developed for efficient siRNA delivery into the cytosol of target cells.[2] Among them, siRNA conjugates have arisen as one of the promising strategies in siRNA delivery, as siRNA can be readily conjugated to a functional molecule to acquire the ability of "programmed transfer" to the target sites.[3] Indeed, several ligand molecules, such as lactose and RGD peptide, were conjugated with siRNA for site- (or cell)-specific delivery.[3] Furthermore, multimolecular siRNA conjugates enable stable polyion complex (PIC) formation because of the increased electrostatic interactions with polycations, leading to facilitated cellular uptake through charge neutralization of siRNA and also protection of siRNA from enzymatic degradations.[4] However, those siRNA conjugates potentially stimulate immune responses through the activation of toll-like receptor 3 and/or protein kinase R,[4,5] and thus they are desired to disintegrate into monomeric siRNAs (mono-siRNAs) in the cell for reduced immune responses.[4] Meanwhile, considering that macromolecular drugs, including siRNA and its conjugates, would be taken up by cells through endocytosis and then delivered to the late endosome toward lysosomal degradation, siRNA needs to escape from the endosome into the cytosol for efficient gene silencing.[6] Therefore, design of a smart siRNA conjugate for programmed endosomal escape and release of mono-siRNA is a great challenge for successful siRNA delivery.

Herein, we developed a smart siRNA conjugate to fulfill the multifunctionality desired for enhanced siRNA delivery with reduced immunogenicity; that is, reversible PIC stability, endosomal escapability, and mono-siRNA releasability, based on a single chemical process. It is known that maleic acid amide (MAA) is relatively stable at extracellular neutral pH, while rapidly hydrolyzed at endosomal acidic pH.[7] Thus, we utilized this MAA chemistry as an acid-labile anionic moiety for linking siRNA to an endosome-disrupting polycation and concurrently converting the cationic sites into a biologically inert anionic derivative.[8] In design, the MAA-based conjugate is expected to improve the PIC stability through increased electrostatic interaction, while degrading the MAA moieties in the endosome for triggering three actions: 1) complex destabilization through unbalanced charges within PICs; 2) endosome disruption with the regenerated parent polycation; and 3) mono-siRNA release by MAA cleavage (Figure 1a). Figure 1b shows the chemical structure of siRNA-releasable/endosome-disrupting conjugate (REC), in which several siRNA molecules are grafted into the endosome-disrupting polymer side chains by the MAA linkage. The parent polycation is a polyaspartamide derivative with two repeating units of aminoethylene in each side chain (termed PAsp(DET)), which destabilizes the endosomal membrane integrity with the cationic diprotonated side chains to accelerate endosomal escape of the payload.[9]

A precursor polyanion was synthesized from PAsp(DET) to have a dibenzyl cyclooctyne (DBCO) group by MAA linkage as a conjugation site for siRNA. Then, an azide-modified siRNA (azide-siRNA) was reacted with the DBCO group in the polyanion side chains. Notably, the size exclusion chromatography (Supporting Information, Figure S5) confirmed that more than 95% of azide-siRNAs were conjugated to the polymer backbone utilizing a freeze–thaw treatment for the generation of a highly concentrated reactant phase.[10] This successful conjugation at the quite high rate allows the use of the obtained conjugate without further purification. As a result, about 30% of DBCO groups in the polymer side chains reacted with azide-siRNA; that is, about 5 siRNAs contained in the conjugate (Figure 1b). To investigate the

[*] H. Takemoto, Dr. K. Kataoka
Department of Materials Engineering, The University of Tokyo
Hongo 7-3-1, Bunkyo-ku, Tokyo 113-8656 (Japan)
E-mail: kataoka@bmw.t.u-tokyo.ac.jp
Homepage: http://www.bmw.t.u-tokyo.ac.jp/
S. Hattori, Dr. T. Ishii, T. Suma
Department of Bioengineering, The University of Tokyo
Hongo 7-3-1, Bunkyo-ku, Tokyo 113-8656 (Japan)
Dr. K. Miyata, S. Uchida
Division of Clinical Biotechnology, Center for Disease Biology and Integrative Medicine, The University of Tokyo
Hongo 7-3-1, Bunkyo-ku, Tokyo 113-0033 (Japan)
E-mail: miyata@bmw.t.u-tokyo.ac.jp
Dr. N. Nishiyama
Polymer Chemistry Division, Chemical Resources Laboratory
Tokyo Institute of Technology, R1-11
4259 Nagatsuta, Midori-ku, Yokohama 226-8503 (Japan)

[**] This research is supported by the Japan Society for the Promotion of Science (JSPS) through the "Funding Program for World-Leading Innovative R&D on Science and Technology (FIRST Program)," and Health and Labour Sciences Research Grants Research on Medical Device Development, Ministry of Health, Labour and Welfare. H.T. thanks the Research Fellowships of the Japan Society for the Promotion of Science for Young Scientists (JSPS).

Supporting information for this article is available on the WWW under http://dx.doi.org/10.1002/anie.201300178.

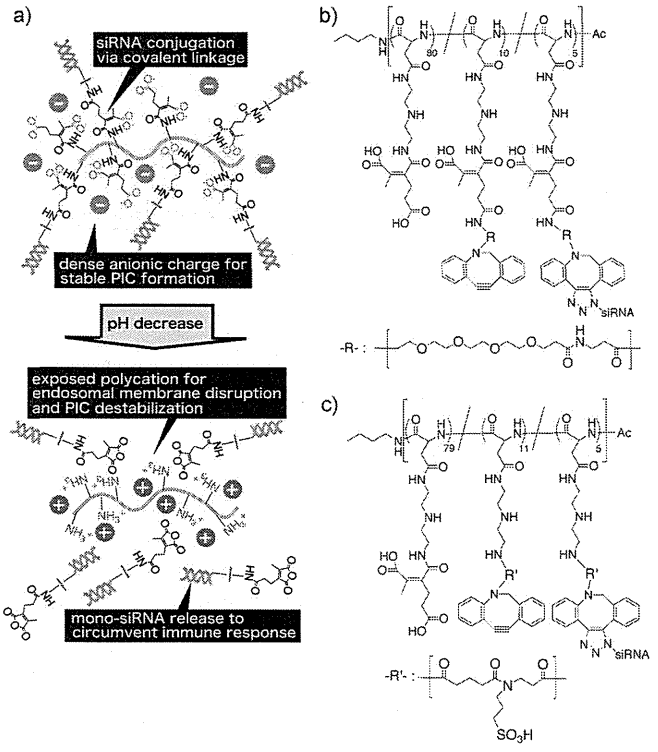

Figure 1. a) Illustration of releasable/enzyme-disrupting conjugate (REC) with the multifunctionality toward endosomal escape and release of mono-siRNA. b) Chemical structure of REC. c) Chemical structure of uREC. The PAsp derivative in this study has the mixed sequence of α and β isomers. Only α isomers are depicted in (b) and (c) for simplicity.

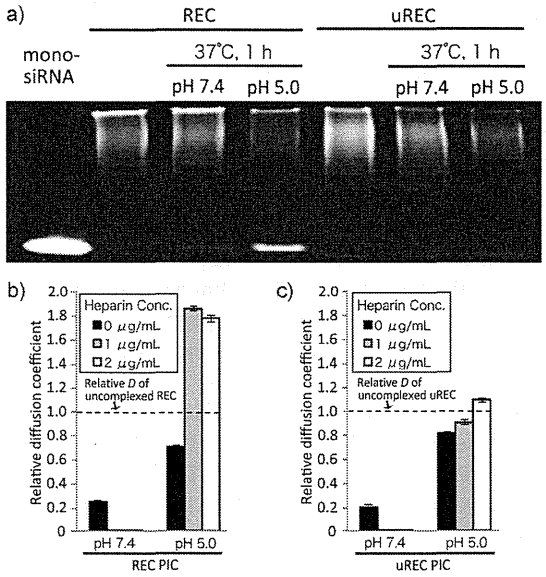

Figure 2. a) PAGE analysis of REC and uREC before and after 1 h incubation at 37 °C and at pH 7.4 or pH 5.0. b),c) Relative *D* values of siRNA conjugate PICs after a 30 min incubation at 37 °C with various heparin concentrations at pH 7.4 or pH 5.0. Relative *D* values are calculated by normalization of *D* to that of uncomplexed siRNA conjugates; REC PIC (b) and uREC PIC (c). Results were shown as mean and standard deviation obtained from 10 measurements.

effect of MAA linkage on the siRNA releasability, another siRNA conjugate, in which the DBCO group was directly conjugated to primary amines in PAsp(DET) without MAA linkage, was also synthesized as an siRNA-unreleasable but endosome-disrupting control (uREC; Figure 1c). The obtained siRNA conjugates were analyzed for their pH-sensitivity by polyacrylamide gel electrophoresis (PAGE) analysis (Figure 2a). The retarded bands in siRNA conjugates, compared to mono-siRNA, indicate that both siRNA conjugates had significantly higher molecular weight than mono-siRNA. A 1 h incubation of REC at pH 5.0 resulted in the band appearance at the same position as mono-siRNA, whereas such band was not observed at pH 7.4, indicating that mono-siRNA release was triggered selectively at the acidic pH. In contrast, the band corresponding to mono-siRNA was not observed for uREC after a 1 h incubation at both pHs of 5.0 and 7.4, indicating the essential role of MAA linkage for mono-siRNA release from REC.

Next, siRNA conjugates were mixed with a polycation PAsp(DET) to form PICs at N/P 10 (residual molar ratio of amines of PAsp(DET) to phosphates of siRNA) for their facilitated cellular uptake. PIC formation with siRNA conjugates as well as mono-siRNA was confirmed by fluorescence correlation spectroscopy (FCS) using Cy3-labeled siRNA (Cy3-siRNA) and its conjugates (Supporting Information, Table S2) as well as agarose gel electrophoresis (Supporting Information, Figure S6). The diffusion coefficients *D* in 10 mM HEPES buffer (pH 7.4) were determined to be 66.2 $\mu m^2 s^{-1}$ for mono-siRNA PIC and 2.9 $\mu m^2 s^{-1}$ for both siRNA conjugate PICs. These values were significantly smaller than those of the uncomplexed controls; that is, mono-siRNA (94.5 $\mu m^2 s^{-1}$) and siRNA conjugates (15.5 $\mu m^2 s^{-1}$ for REC and 18.8 $\mu m^2 s^{-1}$ for uREC). Considering that the *D* value of nanoparticles is inversely correlated with their size,[11] the smaller *D* values in the presence of polycation indicate successful PIC formation with the siRNA conjugates as well as mono-siRNA in the aqueous condition (siRNA concentration: 100 nM). The substantially smaller *D* values of the conjugate PICs, compared to the mono-siRNA PIC, indicate a larger association number of siRNA in the conjugate PICs, which is presumably due to increased anionic charges in the conjugate. Then, the acidic pH-sensitive PIC stability was further evaluated by FCS after a 30 min incubation of PICs at 37 °C in 10 mM HEPES (pH 7.4) and 10 mM MES (pH 5.0) containing heparin. Heparin is a major component of extracellular matrices on cellular surface and probably serves as a strong polyanionic counterpart to induce PIC dissociation.[12] The obtained *D* values of each sample were normalized to that of the corresponding uncomplexed siRNA control; that is, uncomplexed REC for REC PIC, uncomplexed uREC for uREC PIC, and uncomplexed mono-siRNA for mono-siRNA PIC (Figure 2b,c; Supporting Information, Figure S7, respectively). After incubation with heparin, a relative *D* of mono-siRNA PICs progressively increased with the increase in heparin concentration similarly at both pH values of 7.4 and 5.0, indicating that mono-siRNA PICs gradually dissociated with the increased counter polyanion, regardless of the environmental pH (Supporting Information, Figure S7). In contrast, relative *D* values of

REC and uREC PICs decreased after incubation with heparin at pH 7.4, suggesting that the conjugated siRNA is more stably encapsulated within PICs, compared to mono-siRNA, even after binding of heparin onto PIC surface. Notably, the incubation of REC and uREC PICs at pH 5.0 dramatically increased their relative *D* values, and furthermore, the increase in the relative *D* values was facilitated in the presence of heparin, indicating the acidic pH-responsive destabilization of the siRNA conjugate PICs (Figure 2b,c). Considering the fact that the MAA linkage contained in both siRNA conjugates can degrade at pH 5.0 to generate the polycations in PIC, the destabilization of siRNA conjugate PICs at pH 5.0 is presumably due to the electrostatic repulsion between the generated polycations and the originally incorporated polycations in PIC. Furthermore, the increased relative *D* values of REC PICs in the presence of heparin, beyond that of uncomplexed REC, strongly suggest the mono-siRNA release triggered by the cleavage of MAA linkage. These results demonstrate that the acidic pH-sensitivity of the MAA-based conjugates can be maintained even after PIC formation, and also they provide siRNA PICs with a reversible stability in response to the intracellular environment.

Delivery functionalities of REC PICs, namely cellular uptake efficiency and intracellular trafficking profile, were evaluated with cultured human ovarian cancer cells stably expressing luciferase (SKOV3-Luc). Cellular uptake of siRNA was estimated using Cy3-siRNA with a fluorescence microscopy (Supporting Information, Figure S8). REC and uREC PICs (N/P 10) allowed 30% increase in Cy3 fluorescence from cells compared to mono-siRNA PICs (N/P 10, $p < 0.005$), indicating that the conjugate formulation significantly enhanced the cellular uptake of siRNA is probably due to the higher stability, as suggested by the FCS result at pH 7.4 (Figure 2b,c; Supporting Information, Figure S7). Next, confocal laser scanning microscopic (CLSM) observation was performed to examine subcellular distribution of siRNA PICs (N/P 10), especially focusing on the colocalization of siRNA with the late endosome/lysosome as an indicator for endosomal entrapment (Figure 3a–c).[13] In the cells treated with mono-siRNA PICs, the colocalization (yellow) ratio of Cy3-siRNA (red) with a late endosome/lysosome marker LysoSensor Green (green) was increased up to 70% for the initial 12 h and then kept constant for subsequent 36 h (Figure 3d). In contrast, the cells treated with REC and uREC PICs showed that the colocalization ratio was progressively decreased over incubation period and reached about 30% after a 48 h incubation. The significantly lower colocalization ratios (or less endosomal entrapment) of REC/uREC PICs strongly suggest more efficient endosomal escape of siRNA compared to mono-siRNA PICs (Figure 3d). This enhanced endosomal escape with REC and uREC is consistent with the endosome-disrupting functionality of the backbone polymer, which should be converted into the parent polycation PAsp(DET) in the acidic late endosome/lysosome for the membrane disruption, as suggested by a membrane disruption assay at pH 7.4 and 5.0 (Supporting Information, Figure S9).[8,9]

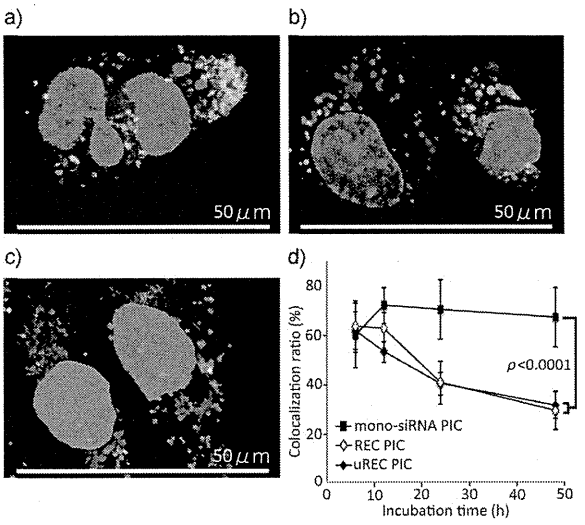

Figure 3. a–c) CLSM images 48 h after treatment of SKOV3-Luc cells with mono-siRNA PIC (a), REC PIC (b), and uREC PIC (c). Red Cy3-siRNA, green late endosome/lysosome (LysoSensor Green), blue nucleus (Hoechst 33342). A yellow pixel indicates colocalization between a red pixel and green pixel. d) Time-dependent change in the colocalization ratio between Cy3-siRNA and late endosome/lysosome. The colocalization ratio was shown as mean and standard deviation obtained from 10 cells. The *p* value was calculated according to Student's *t* test.

Next, the gene silencing ability of REC PICs was compared with mono-siRNA and uREC PICs by luciferase assay with cultured SKOV3-Luc cells (Figure 4a). Obviously, REC and uREC PICs achieved more efficient sequence-specific gene silencing in the cells than mono-siRNA PICs, which is presumably due to the enhanced endosomal escape of siRNA conjugate PICs (Figure 3) as well as facilitated cellular uptake of siRNA (Supporting Information, Figure S8). Interestingly, REC PICs induced significantly stronger gene silencing than uREC PICs ($p < 0.005$), demonstrating the positive effect of siRNA releasability by the MAA linkage on the siRNA delivery functionality. Mono-siRNA

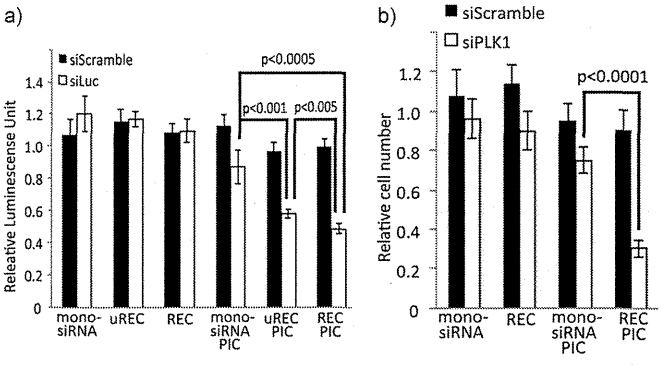

Figure 4. a) Luciferase gene expression in cultured SKOV3-Luc cells after PIC treatment at 100 nM Luc siRNA (siLuc) or scramble siRNA (siScramble) for 48 h. b) Cell viability in cultured A549 cells after PIC treatment at 100 nM PLK1 siRNA (siPLK1) or siScramble for 72 h. In both figures, results were shown as mean and standard deviation obtained from 6 samples. The *p* values were calculated according to Student's *t* test.

releasates from REC might be more readily associated with the gene silencing pathway owing to compromised steric hindrance compared to the conjugated structure. Also, no cytotoxicity was observed for all the tested PIC formulations under the same conditions as the gene-silencing assay (Supporting Information, Figure S10). Significantly stronger luciferase gene silencing of REC PICs was also confirmed in comparison with mono-siRNA PICs prepared with PAsp-(DET)/PAsp(DET-CDM) (a non-covalent control) and a commercially available reagent ExGen500 (linear polyethylenimine; Supporting Information, Figure S11), demonstrating the advantage of REC formulation, including covalent conjugation between siRNA and the backbone polymer. The effect of the siRNA-releasability of REC was further examined from the standpoint of immune responses; IFNα response was determined as an indicator of immune response by enzyme-linked immunosorbent assay (ELISA). REC, uREC, and their PICs did not induce a detectable level of IFNα production for SKOV3-Luc cells ($< 10\,pg\,mL^{-1}$, data not shown). Thus, the similar ELISA experiment was further challenged for murine macrophage cells (Raw264.7), which are known to be highly sensitive to immunogen.[14] As a result, REC PICs induced a significantly lower level of IFNα production ($24.3 \pm 3.5\,pg\,mL^{-1}$) compared to uREC PICs ($60.8 \pm 12.9\,pg\,mL^{-1}$, $p < 0.005$), indicating that the siRNA-releasability based on MAA linkage successfully decreased the immune response for siRNA conjugates. Uncomplexed REC and uREC without polycation did not induce a detectable level of IFNα production, suggesting that they should not stimulate IFNα response at least on the cellular surface. Finally, the utility of REC PICs was verified for other cell lines, using a therapeutic siRNA targeting polo-like kinase 1 (PLK1). PLK1 is known to be a cell cycle regulator, and thus its silencing can arrest the cell cycle toward the apoptosis.[15] REC PICs with PLK1 siRNA (N/P 20) sequence-specifically suppressed the growth of human lung carcinoma cells (A549) and human hepatocarcinoma cells (Huh-7; Figure 4b; Supporting Information, Figure S12, respectively), demonstrating a strong potential of the REC formulation bearing the MAA linkage for siRNA-based cancer therapy.

In summary, an acidic pH-responsive siRNA conjugate was developed for enhanced siRNA delivery with reduced immunogenicity. A single chemical process based on the MAA linkage successfully provided the multifunctionality required for successful siRNA delivery; that is, reversible carrier stability, endosomal escapability, and mono-siRNA releasability. Ultimately, the siRNA conjugate sequence-specifically achieved the significant growth inhibition of cancerous cells. The programmed siRNA delivery based on the smart conjugate will be further investigated for the success in siRNA therapeutics.

Received: January 9, 2013
Revised: February 25, 2013
Published online: April 29, 2013

Keywords: conjugation · drug delivery · drug design · polymers · siRNA

[1] a) S. M. Elbashir, J. Harborth, W. Lendeckel, A. Yalcin, K. Weber, T. Tuschl, *Nature* **2001**, *411*, 494–498; b) J. C. Burnett, J. J. Rossi, *Chem. Biol.* **2012**, *19*, 60–71.
[2] R. L. Kanasty, K. A. Whitehead, A. J. Vegas, D. G. Anderson, *Mol. Ther.* **2012**, *20*, 513–524.
[3] a) D. B. Rozema, D. L. Lewis, D. H. Wakefield, S. C. Wong, J. J. Klein, P. L. Roesch, S. L. Bertin, T. W. Reppen, Q. Chu, A. V. Blokhin, J. E. Hagstrom, J. A. Wolf, *Proc. Natl. Acad. Sci. USA* **2007**, *104*, 12982–12987; b) Y. Singh, P. Murat, E. Defrancq, *Chem. Soc. Rev.* **2010**, *39*, 2054–2070; c) M. R. Alam, X. Ming, M. Fisher, J. G. Lackey, K. G. Rajeev, M. Manoharan, R. L. Juliano, *Bioconjugate Chem.* **2011**, *22*, 1673–1681; d) S. K. Lee, A. Siefert, J. Beloor, T. M. Fahmy, P. Kumar, *Methods Enzymol.* **2012**, *502*, 91–122.
[4] a) A.-L. Bolcato-Bellemin, M.-E. Bonnet, G. Creusat, P. Erbacher, J.-P. Behr, *Proc. Natl. Acad. Sci. USA* **2007**, *104*, 16050–16055; b) H. Mok, S. H. Lee, J. W. Park, T. G. Park, *Nat. Mater.* **2010**, *9*, 272–278; c) H. Takemoto, A. Ishii, K. Miyata, M. Nakanishi, M. Oba, T. Ishii, Y. Yamasaki, N. Nishiyama, K. Kataoka, *Biomaterials* **2010**, *31*, 8097–8105; d) C. A. Hong, S. H. Lee, J. S. Kim, J. W. Park, K. H. Bae, H. Mok, T. G. Park, H. Lee, *J. Am. Chem. Soc.* **2011**, *133*, 13914–13917; e) S. J. Lee, M. S. Huh, S. Y. Lee, S. Min, S. Lee, H. Koo, J. U. Chu, K. E. Lee, H. Jeon, Y. Choi, K. Choi, Y. Byun, S. Y. Jeong, K. Park, K. Kim, I. C. Kwon, *Angew. Chem.* **2012**, *124*, 7315–7319; *Angew. Chem. Int. Ed.* **2012**, *51*, 7203–7207.
[5] A. Judge, I. MacLachlan, *Hum. Gene Ther.* **2008**, *19*, 111–124.
[6] a) C. Troiber, E. Wagner, *Bioconjugate Chem.* **2011**, *22*, 1737–1752; b) J. Nguyen, F. C. Szoka, *Acc. Chem. Res.* **2012**, *45*, 1153–1162.
[7] a) D. B. Rozema, K. Ekena, D. L. Lewis, A. G. Loomis, J. A. Wolff, *Bioconjugate Chem.* **2003**, *14*, 51–57; b) S. Guo, Y. Huang, Q. Jiang, Y. Sun, L. Deng, Z. Liang, Q. Du, J. Xing, Y. Zhao, P. C. Wang, A. Dong, X.-J. Liang, *ACS Nano* **2010**, *4*, 5505–5511.
[8] Y. Lee, K. Miyata, M. Oba, T. Ishii, S. Fukushima, M. Han, H. Koyama, N. Nishiyama, K. Kataoka, *Angew. Chem.* **2008**, *120*, 5241–5244; *Angew. Chem. Int. Ed.* **2008**, *47*, 5163–5166.
[9] K. Miyata, M. Oba, M. Nakanishi, S. Fukushima, Y. Yamasaki, H. Koyama, N. Nishiyama, K. Kataoka, *J. Am. Chem. Soc.* **2008**, *130*, 16287–16294.
[10] H. Takemoto, K. Miyata, T. Ishii, S. Hattori, S. Osawa, N. Nishiyama, K. Kataoka, *Bioconjugate Chem.* **2012**, *23*, 1503–1506.
[11] J. DeRouchey, C. Schmidt, G. F. Walker, C. Koch, C. Plank, E. Wagner, J. O. Radler, *Biomacromolecules* **2008**, *9*, 724–732.
[12] a) M. J. Palte, R. T. Raines, *J. Am. Chem. Soc.* **2012**, *134*, 6218–6223; b) M. Zheng, D. Librizzi, A. Kılıç, Y. Liu, H. Renz, O. M. Merkel, T. Kissel, *Biomaterials* **2012**, *33*, 6551–6558.
[13] K. Whitehead, G. Sahay, G. Z. Li, K. T. Love, C. A. Alabi, M. Ma, C. Zurenko, W. Querbes, R. S. Langer, D. G. Anderson, *Mol. Ther.* **2011**, *19*, 1688–1694.
[14] J. Turco, H. H. Winker, *Infect. Immun.* **1982**, *35*, 783–791.
[15] a) A. D. Judge, M. Robbins, I. Tavakoli, J. Levi, L. Hu, A. Fronda, E. Ambegia, K. McClintock, I. MacLachlan, *J. Clin. Invest.* **2009**, *119*, 661–673; b) K. Strebhardt, *Nat. Rev. Drug Discovery* **2010**, *9*, 643–660.

Biomaterials 34 (2013) 562–570

Contents lists available at SciVerse ScienceDirect

Biomaterials

journal homepage: www.elsevier.com/locate/biomaterials

Silica nanogelling of environment-responsive PEGylated polyplexes for enhanced stability and intracellular delivery of siRNA

Noha Gouda [a,b], Kanjiro Miyata [c,**], R. James Christie [c], Tomoya Suma [a], Akihiro Kishimura [d], Shigeto Fukushima [d], Takahiro Nomoto [a], Xueying Liu [c], Nobuhiro Nishiyama [c], Kazunori Kataoka [a,c,d,e,*]

[a] Department of Bioengineering, Graduate School of Engineering, The University of Tokyo, 7-3-1 Hongo, Bunkyo-ku, Tokyo 113-8656, Japan
[b] Department of Pharmaceutics, Faculty of Pharmacy, Alexandria University, Azarita, Khartoum square, Alexandria 21521, Egypt
[c] Center for Disease Biology and Integrative Medicine, Graduate School of Medicine, The University of Tokyo, 7-3-1 Hongo, Bunkyo-ku, Tokyo 113-0033, Japan
[d] Department of Materials Engineering, Graduate School of Engineering, The University of Tokyo, 7-3-1 Hongo, Bunkyo-ku, Tokyo 113-8656, Japan
[e] Center for NanoBio Integration, The University of Tokyo, 7-3-1 Hongo, Bunkyo-ku, Tokyo 113-8656, Japan

ARTICLE INFO

Article history:
Received 16 August 2012
Accepted 29 September 2012
Available online 17 October 2012

Keywords:
siRNA delivery
Polyplex
Silica
PEG
Disulfide cross-link

ABSTRACT

In this study, poly(ethylene glycol) (PEG)-block-polycation/siRNA complexes (PEGylated polyplexes) were wrapped with a hydrated silica, termed "silica nanogelling", in order to enhance their stability and functionality. Silica nanogelling was achieved by polycondensation of soluble silicates onto the surface of PEGylated polyplexes comprising a disulfide cross-linked core. Formation of silica nanogel layer on the PEGylated cross-linked polyplexes was confirmed by particle size increase, surface charge reduction, and elemental analysis of transmission electron micrographs. Silica nanogelling substantially improved polyplex stability against counter polyanion-induced dissociation under non-reductive condition, without compromising the reductive environment-responsive siRNA release triggered by disulfide cleavage. Silica nanogelling significantly enhanced the sequence-specific gene silencing activity of the polyplexes in HeLa cells without associated cytotoxicity, probably due lower endosomal entrapment (or lysosomal degradation) of delivered siRNA. The lower endosomal entrapment of the silica nanogel system could be explained by an accelerated endosomal escape triggered by deprotonated silanol groups in the silica (the proton sponge hypothesis) and/or a modulated intracellular trafficking, possibly *via* macropinocytosis, as evidenced by the cellular uptake inhibition assay. Henceforth, silica nanogelling of PEGylated siRNA polyplexes is a promising strategy for preparation of stable and functional siRNA delivery vehicles.

1. Introduction

Small interfering RNA (siRNA) has opened wide new horizons for therapeutic mechanisms for a variety of intractable diseases [1–3], as it can induce potent sequence-specific gene silencing, termed RNA interference (RNAi) [4]. However, when administered in the body, siRNA is susceptible to degradation by serum nucleases and to rapid elimination *via* the kidneys. These inherent drawbacks of siRNA substantially compromise its *in vivo* gene silencing activity, hence necessitating the use of carrier systems for its successful delivery to the cytoplasm of target cell. Examples of the types of carrier systems that have been developed for siRNA delivery include: cationic lipid-based complexes (lipoplexes) [5–8], polycation-based complexes (polyplexes) [9–17], inorganic nanoparticles [18–20], and their hybrid systems [21–24]. Nevertheless, there is still a great need for more efficient and safer carrier formulations for clinical application of siRNA therapeutics.

One promising approach for development of siRNA carriers is to construct environment-responsive nanoparticles that stably enclose siRNA while in extracellular conditions protecting it from enzymatic degradation and renal clearance, whereas releasing siRNA in the cytoplasm of target cells to induce RNAi. For this purpose, intracellularly cleavable linkers, such as the disulfide bond, have been integrated into carrier components to provide polyplexes with the reversible stability in response to cytoplasmic reducing potential [25]. Previous studies have reported the cross-linking of poly(ethylene glycol)-modified (PEGylated) polyplexes by environment-

* Corresponding author. Department of Bioengineering, Graduate School of Engineering, The University of Tokyo, 7-3-1 Hongo, Bunkyo-ku, Tokyo 113-8656, Japan. Tel.: +81 3 5841 7138; fax: +81 3 5841 7139.
** Corresponding author. Tel.: +81 3 5841 1701; fax: +81 3 5841 7139.
E-mail addresses: miyata@bmw.t.u-tokyo.ac.jp (K. Miyata), kataoka@bmw.t.u-tokyo.ac.jp (K. Kataoka).

0142-9612/$ – see front matter © 2012 Elsevier Ltd. All rights reserved.
http://dx.doi.org/10.1016/j.biomaterials.2012.09.077

responsive disulfide bonds for enhanced stability and biocompatibility in extracellular non-reductive conditions [26–29]. The obtained PEGylated cross-linked polyplexes (PCPs) successfully improved the gene silencing activity in cultured cells. Nevertheless, the PCPs apparently require further stabilization for the longevity in the bloodstream, as their blood half-life was still less than 15 min, although it was significantly longer than naked siRNA [28].

A major mechanism for polyplex destabilization/dissociation in the body is counter polyanion exchange reaction between polyplexes and negatively charged biomacromolecules, such as albumin and heparan sulfate. These biomacromolecules can directly bind to the polyplex-forming polycations to form ion pairs, resulting in release of free siRNA. Non-ionic, hydrophilic, and highly flexible PEG shielding is one of the approaches commonly used to reduce non-specific interactions of polyplexes with biomacromolecules [30–32], however additional surface shielding is still needed for complete inhibition of those undesired interactions. In this regard, we focused on silica nanogel shielding of polyplexes using soluble silicates; the silica nanogel layer can be formed directly on the polyplex surface through condensation of anionic silicic acid species in the vicinity of polycations [33–36] to form a gel layer sufficiently covering the net positive charge of polyplexes (Fig. 1). The resulting silica gel layer can be gradually degraded in dilute conditions into small silicate species [37], which are readily excreted *via* the kidneys [38]. Indeed, our recent study demonstrated that the anionic silica layer was successfully prepared on non-PEGylated siRNA polyplex surface, transiently stabilizing the polyplex structure and allowing additional surface modification with polycationic materials by a layer-by-layer technique toward multifunctional siRNA delivery [36].

In the present study, the silica nanogelling was utilized to wrap the siRNA PCPs equipped with PEG palisade in order to improve their stability and functionality. The outer silica nanogel layer provided a negatively charged protective shell surrounding the PCPs minimizing their vulnerability against the polyanion-induced dissociation under non-reductive conditions. Meanwhile, the disulfide cleavage in the polyplex core compromised the protective effect of silica nanogelling, leading to the selective release of the siRNA payload under reductive conditions, such as the cytoplasm. The formation of a silica nanogel layer on the PCP surface was verified from the change in size and surface charge, as well as from elemental mapping by energy dispersive X-ray (EDX) analysis measured by scanning transmission electron microscopy (STEM). Furthermore, effect of reversible stability of polyplexes was examined on siRNA release under non-reductive and reductive environments. The biological effect of the silica nanogel wrapping on gene silencing activity in cultured cancer cells, and also the effect on transfection mechanisms, including cellular uptake, endocytic pathway, and intracellular trafficking, were investigated. Ultimately, it was demonstrated that the silica nanogelling is a promising approach for reversible stabilization and functionalization of PCPs toward enhanced siRNA delivery.

2. Materials and methods

2.1. Materials

Firefly GL3 luciferase siRNA (siGL3) (sense: 5′-CUU ACG CUG AGU ACU UCG AdTdT-3′; antisense: 5′-UCGAAG UAC UCA GCG UAA GdTdT-3′), Cy5-labeled siGL3 (Cy5-siGL3), and scramble siRNA (siSCR) (sense: 5′-UUC UCC GAA CGU GUC ACG UdTdT-3′; antisense: 5′-ACG UGA CAG GUU CGG AGA AdTdT-3′) were synthesized by Hokkaido System Science Co., Ltd. (Hokkaido, Japan). The block copolymer, poly(ethylene glycol)-*block*-poly(L-lysine) (PEG-PLL) was synthesized as previously described [39]. Sodium silicate solution reagent grade (~27% SiO_2), Dulbecco's modified Eagle's medium (DMEM), trypsine-ethylenediaminetetraacetate (EDTA) solution (10×), Amiloride hydrochloride hydrate, dithiothreitol (DTT), and chlorpromazine hydrochloride were purchased from Sigma Aldrich Co. (St. Louis, MO, USA). Dimethyl sulfoxide (DMSO) was purchased from Tokyo Chemical Industry Co. Ltd. (Tokyo, Japan). Sterile HEPES (1 M, pH 7.3) was purchased from Amresco (Solon, OH, USA) and used as a buffer solution after dilution with ultrapure water. DTT (molecular biology grade DNase and RNase free), sodium dextran sulfate (Mw = 5000 Da), and phosphate buffered saline (PBS) were purchased from Wako Pure Chemical Industries Ltd. (Osaka, Japan). The luciferase-expressing human cervical cancer cell line, HeLa-Luc, was purchased from Caliper LifeScience (Hopkinton, MA, USA). Fetal bovine serum (FBS) was purchased from Dainippon Sumitomo Pharma Co., Ltd. (Osaka, Japan). Luciferin as a substrate for luciferase was purchased from Summit Pharmaceutical International (Tokyo, Japan). 10 × TBE running buffer was purchased from Invitrogen (Carlsbad, CA, USA). SYBR Green II and agarose were purchased from Takara Bio (Shiga, Japan). Luciferase Assay System Kit was purchased from Promega Co. (Madison, WI, USA). ExGen500 was purchased from Fermentas Life Sciences (Burlington, Canada). Dimethyl 3,3′-dithiobispropionimidate.HCl (DTBP) and slide-a-lyzer dialysis cassettes (MWCO = 3500 Da) were obtained from Thermo Scientific (Rockford, IL, USA).

2.2. Synthesis of PEG-PLL(MPA)

PEG-PLL bearing 1-(3-mercaptopropyl)amidine (MPA) groups in the lysine side chains (PEG-PLL(MPA)) was synthesized by the reaction of lysine primary amines with imidoesters of DTBP (Supporting Scheme 1), as previously described [28]. PEG-PLL (Mw of PEG = 12000; degree of polymerization (DP) of PLL = 88) (300 mg, 0.6 mmol amine) was dissolved in 200 mM sodium borate, pH 9.0 (60 mL) before adding DTBP (308 mg, 1.4 mmol, 1.5 equiv relative to lysine amines). The reaction was stirred at room temperature for 45 min, transferred to slide-a-lyzer dialysis cassettes, and then dialyzed against 10 mM phosphate buffer with 150 mM NaCl (pH 7.4) for 1.5 h to remove unreacted DTBP. After the recovery of the reaction mixture, DTT (300 mg) was added in order to generate thiol groups in the polymer side chains. The reaction was stirred at room temperature for 30 min before being transferred to slide-a-lyzer dialysis cassettes to perform dialysis against 10 mM phosphate buffer containing 150 mM NaCl (pH 6.0) for 2 h and distilled water for another 2 h with rapid stirring. The dialyzed polymer solution was passed through a 0.2 μm filter and lyophilized to obtain PEG-PLL(MPA) as a chloride salt form (299 mg, yield: 83%). The substitution degree of DTBP in the PLL side chain was determined to be 90% from the ^{1}H NMR spectrum based on the peak intensity ratio of the β, γ, and δ-methylene protons of Lys (–$(CH_2)_3$–, δ = 1.3–1.9 ppm) to the protons of mercaptoethyl groups (HS–$(CH_2)_2$–, δ = 2.7–2.9 ppm) (Supporting Fig. 1).

2.3. Preparation of PEGylated cross-linked polyplexes (PCPs) and their silica nanogelling

PCPs were prepared following the previously established protocol [28]. PEG-PLL(MPA) was dissolved in 10 mM HEPES buffer (pH 7.4) to produce a 5 mg/mL polymer stock solution having 12.9 mM of amidine groups. For complexation with siRNA (Mw = ~13000 Da), an aliquot of the stock solution was diluted with 10 mM HEPES buffer (pH 7.4) and then mixed with the same volume of 10 mM HEPES buffer (pH 7.4) containing 200 mM DTT. The polymer solution was incubated for 30 min at

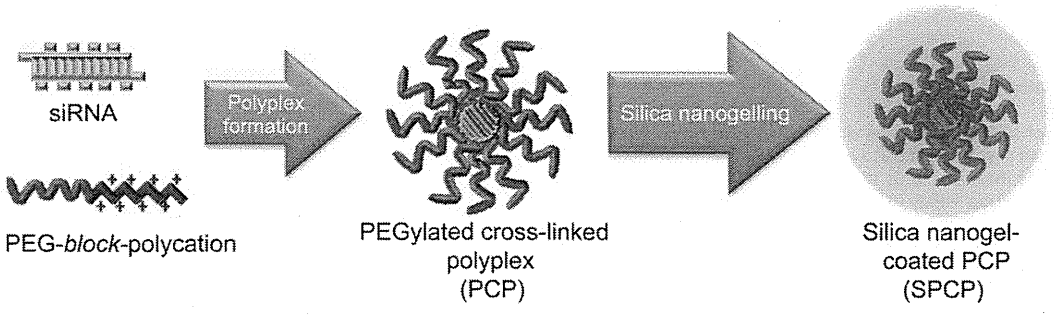

Fig. 1. Schematic illustration of preparation of PEGylated cross-linked polyplexes (PCPs) as a platform and their silica nanogelling for construction of silica nanogel-coated PCPs (SPCPs).

room temperature to ensure reduction of any disulfide bonds present in the MPA moieties. The reduced polycation solution was then mixed with two-fold excess volume of siRNA (15 μM) dissolved in the same buffer at a mixing residual molar ratio (N/P ratio) of primary amines and amidines in PEG-PLL(MPA) to phosphates in siRNA = 1.7. To facilitate disulfide cross-linking in polyplexes, dialysis (slide-a-lyzer cassette) was performed against 10 mM HEPES buffer (pH 7.4) containing 0.5% v/v DMSO for 2 days, followed by another 2 days of dialysis against 10 mM HEPES buffer (pH 7.4) for removal of DMSO. The obtained PCP solution was mixed with the same volume of sodium silicate solutions (0–60 mM silicate) in 10 mM HEPES buffer (pH 7.4) (a final siRNA concentration: 5 μM), and incubated for 24 h before use. Prior to silica nanogelling, the silicate solutions were prepared by diluting a sodium silicate stock solution (~27% SiO_2) with 10 mM HEPES buffer, and final pH (pH 7.4) was adjusted with HCl. Silica nanogel-coated PCPs are abbreviated as SPCP-X (X represents a silicate concentration (mM) in preparation).

2.4. Dynamic light scattering (DLS) and ζ-potential measurements

DLS and ζ-potential measurements were performed at a temperature of 25 °C and a detection angle of 173° with a Zetasizer Nano ZS instrument (Malvern Instruments Ltd., Worcestershire, UK) equipped with a He-Ne laser ($\lambda = 633$ nm) as the incident beam. For DLS measurements, 20 μL samples of PCP or SPCP in a 10 mM HEPES buffer (pH 7.4) were loaded into a Zen 2112 low-volume cuvette 24 h after preparation. The diffusion coefficient (D_C) of samples, calculated based on the data regarding the decay in the photon correlation function, was converted to the hydrodynamic diameter (D_H) using the Stokes-Einstein equation,

$$D_H = k_B T / 3\pi\eta D_C,$$

where T is the absolute temperature, k_B is the Boltzmann constant, and η is the viscosity of the buffer.

For ζ-potential measurements, 800 μL of sample solutions were put into a folded capillary cell (Malvern Instruments, Ltd.). The ζ-potential (ζ) was calculated from the obtained electrophoretic mobility (v) by applying the Smoluchowski equation

$$\zeta = 4\pi\eta\nu/\varepsilon,$$

where η is the viscosity of the solvent, ν is the electrophoretic mobility, and ε is the dielectric constant of the solvent.

2.5. Scanning transmission electron microscope (STEM)-energy dispersive X-ray (EDX) (STEM-EDX) analysis

STEM-EDX analysis was performed on a 200-keV field-emission gun (FEG) microscope JEOL JEM 2100F (JEOL Ltd., Tokyo, Japan) equipped with a JED-2300T EDX analyzer (JEOL Ltd., Tokyo, Japan). Aqueous aliquots of samples (2 μL) were negatively stained by mixing with 2 μL of uranyl acetate solution (2% w/v in ethanol), then placed on a hydrophilic treated Formvar/carbon-coated copper grid of 400 mesh size (JEOL Ltd., Tokyo, Japan) for 30–45 s before being dried by osmosis against a filter paper at room temperature. Staining was utilized in order to prevent excessive charging and decomposition of the sample under the electron beam. Data were first collected using objective aperture to get bright field (BF) images using an electron beam of 1.5 nm diameter probe with a current of 125 μA, a collection time of 30 s, and 25 scans. For the EDX analyses, the same microscope mode was used, except that objective aperture was eliminated to permit the diffused X-rays to be collected by the EDX detector: 30 mm^2 SDD (silicone drift detector) type with active drift compensation through the microscope control software "Analysis software" (JEOL Ltd., Tokyo, Japan). EDX data were acquired in the approximate 0–10 keV range in 0.01 keV increments. The electron generated X-ray emission peaks occur in the following sequence: C Kα 0.277 keV, N Kα at 0.392 keV, O Kα at 0.525 keV, Si Kα at 1.739 keV, P Kα at 2.013 keV, and S Kα at 2.307 keV. The EDX data were taken as a 256 × 256 pixel, 600 × 600 nm spectrum image with 0.5 ms dwell time per pixel. The EDX spectra were fitted quantitatively using the "Analysis station" software (JEOL Ltd., Tokyo, Japan).

2.6. Agarose gel retardation assay

Polyplex stability (or siRNA release) was examined by agarose gel electrophoresis after incubation with dextran sulfate as a counter polyanion. Samples prepared at 5 μM siRNA (2 μL) was incubated with 10 mM HEPES buffer (pH 7.4) solutions containing 15% glycerol, dextran sulfate (0, 15.6, 31.2, or 46.8 μg/mL), and DTT (0 or 200 mM) (4 μL) for 1 h. Each mixture containing 111 ng siRNA (5 μL) was then loaded onto 1 wt% agarose gel. After electrophoresis at 100 V for 30 min using 1 × TBE running buffer, the gel was stained using ethidium bromide (0.5 mg/L). The gel was visualized at 488 nm for excitation and 620 nm for emission using Typhoon 9410 Gel and Blot Imager (GE Healthcare UK Ltd., England) equipped with the scan control software.

2.7. Time-dependent gene silencing assays

Time-dependent gene silencing activity of polyplexes in cultured cells were determined using AB-2550 Kronos Dio (Atto, Tokyo, Japan), which enables measurement of luminescence emitted from luciferase-expressing cells every 10 min. HeLa-Luc cells were seeded on a 35-mm dish at 25000 cells/well in 2 mL of DMEM containing 10% FBS. After 24 h incubation, the medium was replaced with a fresh medium containing 10% FBS and 100 μM luciferin as a substrate. Each polyplex solution containing 5 μM siGL3 or siSCR was then added to the cells at a final concentration of 100 nM siRNA/well, followed by the luminescence measurement using the Kronos equipment according to the manufacturer's protocol. The results are presented as mean and standard error of the mean obtained from 4 samples.

2.8. Cell viability assay

HeLa-Luc cells were plated onto 96-well plates (10000 cells/well), followed by 24 h incubation in DMEM containing 10% FBS (0.1 mL/well) before replacing with a fresh one. Varying concentrations of SPCP-30 containing siSCR were added to wells at siRNA concentrations ranging between 0 and 500 nM. After 24 h incubation, the cell viability was analyzed using a Cell Counting Kit (CCK)-8 (DOJINDO Laboratories, Kumamoto, Japan), following the manufacturer's protocol. CCK-8 represents a sensitive colorimetric assay for the determination of the number of viable cells based on the reduction of the highly water-soluble tetrazolium salt: WST-8 [2-(2-methoxy-4-nitrophenyl)-3-(4-nitrophenyl)-5-(2,4-disulfophenyl)-2H-tetrazolium, monosodium salt] by dehydrogenases in living cells to give a yellow colored product (formazan). The amount of the formazan dye generated by the activity of dehydrogenases in cells is directly proportional to the number of living cells. The absorbance in each well was measured using a microplate reader (Model 680, BIO-RAD, Hercules, CA, USA). The cell viability in each well was calculated from the obtained values as a percentage of non-treated control wells. The results are presented as mean and standard error of the mean obtained from 8 samples.

2.9. Cellular uptake studies by flow cytometry

The amount of siRNA taken up by HeLa-Luc cells was analyzed by flow cytometry (FCM). HeLa-Luc cells were seeded onto 12-well culture plates (20000 cells/well), followed by 24 h incubation in DMEM containing 10% FBS (1 mL/well). After replacing the medium with fresh one, PCP or SPCP-30 with Cy5-siGL3 was applied to each well at 300 nM siRNA. After 3, 12, and 24 h incubation, cells were rinsed three times with PBS and collected by trypsinization. The collected cells were centrifuged at 1000 g for 2 min and resuspended in PBS. The fluorescence intensity was detected using a BD LSR II instrument (BD Biosciences, Franklin Lakes, NJ, USA) equipped with FACS DIVAsoftware (BD Biosciences). Detection of Cy5 fluorescence was achieved using a 640 nm laser for excitation and a 675 nm long-pass filter for emission. The results are presented as a mean and standard deviation obtained from three samples. For inhibition assays for polyplex endocytosis, the predetermined amount of an endocytic inhibitor, amiloride (1.5 mM), was added to the medium. After 30 min incubation, PCP or SPCP-30 with Cy5-siGL3 was applied to each well at 300 nM siRNA, followed by the similar protocol described above.

2.10. Confocal laser scanning microscope (CLSM) observation

Intracellular distribution studies of PCP and SPCP-30 carrying Cy5-siGL3 were carried out in the presence of a late endosome/lysosome marker, LysoTracker Green. HeLa-Luc cells were plated on a 35 mm glass-based dish at 100000 cells/mL and immersed in DMEM containing 10% FBS. After 24 h incubation, the culture medium was replaced with a fresh one, and the polyplex solution was added at 100 nM siRNA. At 30 min before visualization by LSM780 equipped with the software Zen 2010 with a 63 × objective C-Apochromat (Carl Zeiss, Oberkochen, Germany), Hoechst 33342 (blue) and LysoTracker Green (green) were added at the predetermined concentrations. To evaluate the intracellular distributions of siRNA delivered by polyplexes, CLSM images were taken at different time intervals, and further the colocalization rate of Cy5-siGL3 with the markers was quantified as follows:

$$\text{Colocalization rate}(\%) = \left(\sum \text{Cy5 pixels}_{\text{colocalized}} / \sum \text{Cy5 pixels}_{\text{total}}\right) \times 100,$$

where $\text{Cy5 pixels}_{\text{colocalized}}$ represent the number of Cy5 pixels colocalizing with the marker, and $\text{Cy5 pixels}_{\text{total}}$ represent the number of all Cy5 pixels. The results are presented as mean and standard error of the mean obtained from 25 cells.

2.11. Statistical analysis

The p value was determined by the Student's t-test. The $p < 0.05$ was considered as statistically significant.

3. Results & discussion

3.1. Synthesis of PEG-PLL(MPA)

The synthesis of PEG-PLL(MPA) was performed by the modification of PEG-PLL (Mw of PEG: 12000; DP of PLL: 88) with DTBP in a borate buffer (pH 9.0), in which the primary amino groups of the lysine side chains reacted with imidoester groups contained in DTBP to form amidine groups, with a concomitant release of methanol. An excess molar amount of DTBP (3 equivalents to lysine amines) was used to reduce the polymer–polymer cross-linking, and then unreacted DTBP in the reaction mixture was removed by dialysis. Reduction of the polymer with DTT resulted in cleavage of the internal disulfides and generation of the MPA moiety in the PLL segment. Successful modification of lysine amines with DTBP was confirmed in the ^{1}H NMR spectrum (Supporting Fig. 1), as indicated by the downfield shift of lysine ε-CH_2 groups and the appearance of two methylene peaks corresponding to those found in DTBP. The substitution degree of MPA modification was calculated to be approximately 90% from the peak intensity ratios of the β, γ, and δ-methylene protons of lysine ($-(CH_2)_3-$, δ = 1.3–1.9 ppm) to the protons of mercaptoethyl groups ($HS-(CH_2)_2-$, δ = 2.7–2.9 ppm).

3.2. Preparation of silica nanogel-coated PEGylated cross-linked polyplexes (SPCPs)

Preparation of SPCPs was performed by a two-step protocol. First, platform PCPs were prepared, followed by their silica nanogelling, as illustrated in Fig. 1. As previously reported, the block copolymer PEG-PLL(MPA) can form a core–shell type of cross-linked polyplexes with siRNA at residual molar ratios of [amidines and primary amines in PEG-PLL(MPA)] to [phosphates in siRNA] ranging from 1.1 to 1.9, relatively close to the charge stoichiometric point [28]. Herein, the PCP prepared at the residual molar ratio of 1.7 was selected as a platform for the silica nanogelling, because it possesses slightly positive surface charges (+10.1 mV in ζ-potential) to facilitate the condensation and polymerization of anionic silicates (Table 1).

PCP solutions were mixed with the same volume of sodium silicate solutions (pH 7.4) ranging from 0 to 60 mM to produce SPCPs as well as a control PCP at final concentrations of 0, 5, 10, 20, and 30 mM in silicates and 5 μM in siRNA. Noteworthy, sodium silicate solutions adjusted to a neutral pH contain the readily condensable silicates, $SiO(OH)_3^-$, and orthosilicic acid, $Si(OH)_4$, as major components [35]. As summarized in Table 1, the DLS analysis revealed that the size and PdI of the platform PCP were affected by the silicate concentration in preparation. Particle size drastically increased at 5 mM silicate achieving micron size with a large PdI (>0.3). In contrast, an increase in silicate concentration dramatically reduced particle size, ultimately reaching <150 nm with a lower PdI of ~0.20 (>10 mM silicate). Also, the intensity histograms in DLS revealed a unimodal size distribution of SPCP-30 with a larger size and a slightly larger peak width, compared to that of PCP (Fig. 2). The increase in size, compared to the platform PCP, strongly suggests the generation of the silica nanogel layer surrounding the PCP. The micron sized particle obtained with SPCP-5 are likely the result of secondary aggregate formation between incompletely (or partially) silica-coated polyplexes featuring compromised colloidal stability (or decreased electrostatic and/or steric repulsive force) [35,36,40]. The partial silica nanogelling is suggested by the nearly neutral ζ-potential values of SPCP-5 and SPCP- (~+0.2 mV) (Table 1), which is in between positively charged PCP (~+10 mV) and negatively charged SPCP-20 and SPCP-30 (~−15 mV). The considerably negative ζ-potential values observed for SPCP-20 and SPCP-30 suggest successful silica nanogelling of PCP, as silica nanoparticles possess a significant negative surface charge at a neutral pH [35,36,40]. Apparently, the higher concentrations of silicates in polyplex solutions provided more uniform and thicker silica nanogel layer to the PCP. In this regard, even higher silicate concentrations, *e.g.*, 120 mM silicate for SPCP-60, caused gelation of the entire solutions before mixing with polyplex solutions. Thus, considering the previous result that the silica-coated polyplexes (encapsulating plasmid DNA) prepared at 30 mM silicate achieved the highest gene expression in cultured cells [35], the SPCP-30 formulation was selected as a representative for the following detailed physicochemical and biological characterizations.

Table 1
Hydrodynamic diameter (D_H), polydispersity index (PdI), and ζ-potential of PCP and SPCPs prepared at varying silicate concentrations. The values are presented as mean and standard deviation from three samples except for D_H and PdI of SPCP-5.

Sample	Silicate Conc. (mM)	D_H (nm)	PdI	ζ-Potential (mV)
PCP	0	54.6 ± 1.5	0.09 ± 0.01	+10.1 ± 1.1
SPCP-5	5	15910	0.304	+0.2 ± 0.1
SPCP-10	10	99.2 ± 7.7	0.40 ± 0.01	+0.2 ± 0.2
SPCP-20	20	127.5 ± 2.3	0.19 ± 0.01	−15.1 ± 1.0
SPCP-30	30	139.6 ± 4.1	0.20 ± 0.01	−15.6 ± 1.0

3.3. STEM-EDX analysis

In order to gain direct evidence of silica nanogelling onto PCP, the spatial distribution of the major elemental components in SPCP-30 was investigated by a STEM-EDX analysis and compared to PCP. The STEM-EDX is an advanced microscopic technique that can be used for elemental analysis of flat thin specimen (<10 nm) chiefly in comparison with standard controls for the specimen examined. The BF images were firstly taken for both polyplexes. The obtained BF images display spherical nanoparticles with a diameter of ~30 nm for PCP (Fig. 3A) and ~50 nm for SPCP-30 (Fig. 3B), which are in good agreement with the number-based histograms in DLS measurements (Supporting Fig. 2).

Far away from being a flat thin specimen, such shape and size render the nanoparticles to be considered as thick specimens for EDX, where the point analysis and elemental mapping can be

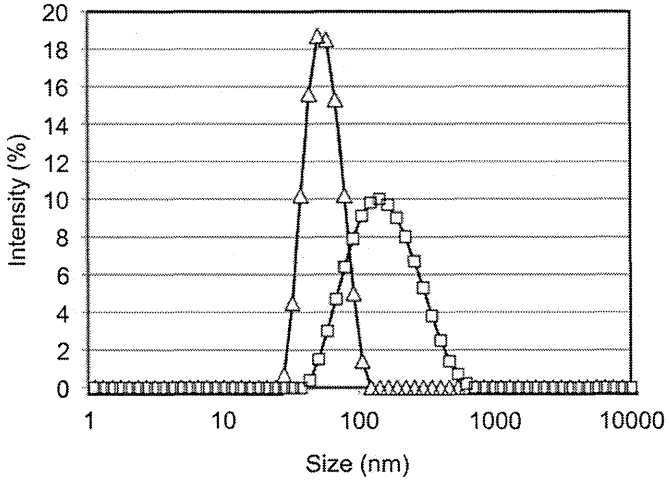

Fig. 2. Intensity-based DLS histograms of PCP (open triangle) and SPCP-30 (open square) (5 μM siRNA).

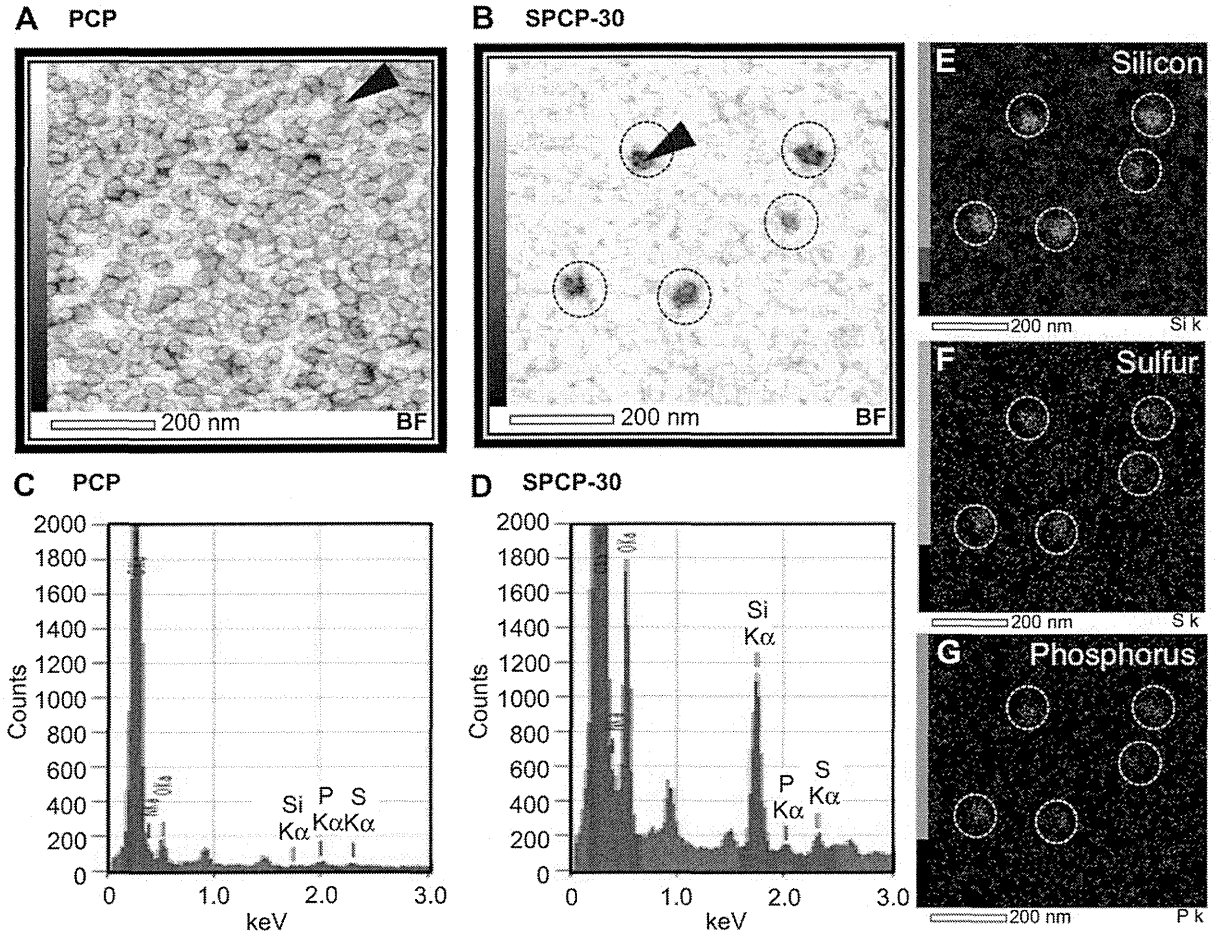

Fig. 3. Bright field (BF) images of PCP (A) and SPCP-30 (B) obtained by STEM, representative EDX spectra of PCP (C) and SPCP-30 (D) taken at the points on the specimen indicated by arrows, and 2-dimensional element maps of SPCP-30 for silicon (E), sulfur (F), and phosphorus (G).

obtained from only the outer surface. Accompanied by the difficulty of preparing standard controls, element quantitative estimation becomes therefore irrelevant in computing the exact composition of the nanoparticles. However, ratios between the different elements can be used to get an approximate estimation about the relative composition of the polyplex surface. Fig. 3C and D display the EDX spectra obtained based on the JEOL 2100F TEM microscope, where the 1.5 nm electron beam was positioned on the center of the nanoparticles, and a total of 20 nanoparticles per each specimen were assessed for the element composition. The 3 major elements that concern the SPCP formulation are: phosphorus contained in siRNA, sulfur contained in PEG-PLL(MPA) side chains, and silicon contained in the silica gel layer. Note that carbon, oxygen, and nitrogen atoms are common in siRNA and the polymer backbone as well as the staining medium used in the specimen preparation; therefore, these signals were not considered for analysis. The comparison between Fig. 3C and D reveals that a relative peak intensity of silicon was obviously magnified in SPCP-30, and also the count ratios of silicon to phosphorus (Si/P) and sulfur (Si/S) show a substantial increase in the silicon content in SPCP-30 (Table 2). Furthermore, the 2-dimensional element maps of SPCP-30 (Fig. 3E–G) clearly display the colocalization of silicon with sulfur and phosphorus as well as the nanoparticles in the BF images. Altogether, these results demonstrate that the silica nanogel layer was deposited onto the PCPs composed of siRNAs and thiolated cationic polymers.

3.4. Reductive environment-responsive stability of PCP and SPCP

Polycations contained in the core of polyplexes may have non-specific interactions with negatively charged biological components to form alternative ion pairs to siRNA phosphates, that is the counter polyion exchange reaction, leading to destabilization of polyplexes or ultimately release of the siRNA payload once exposed to complex biological milieu. This counter polyanion-induced destabilization is a major limitation for effective systemic delivery of siRNA. Hence, the stabilization effect of silica nanogelling against counter polyanion exchange was investigated by agarose gel electrophoresis. This stability assay was executed with or without a reducing reagent DTT, which can imitate intracellular reductive environments, for confirming the reversible stability of polyplexes *via* disulfide bonds. Fig. 4A and B clearly show siRNA release from the PCPs after incubation with dextran sulfate, regardless of DTT. In contrast, SPCP-30 did not show the released siRNA bands in the absence of DTT (Fig. 4A), indicating substantial protective effect of the silica nanogelling to retain siRNA within polyplex structures. On

Table 2
Silicon contents normalized by sulfur and phosphorus on PCP and SPCP-30 in the STEM-EDX analysis. The values are presented as mean and standard error of the mean from 20 nanoparticles.

Sample	Si/S	Si/P
PCP	0.21 ± 0.11	0.28 ± 0.12
SPCP-30	6.56 ± 0.57	31.06 ± 3.53

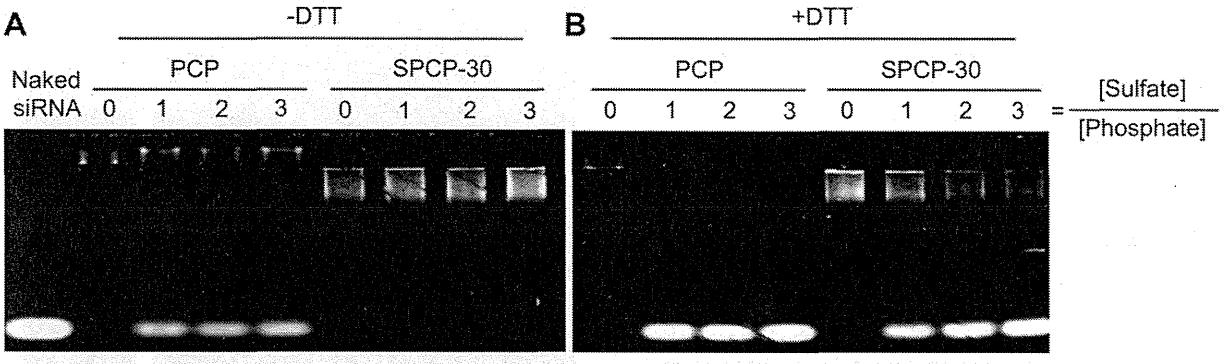

Fig. 4. Gel retardation analysis of PCP and SPCP-30 after incubation with dextran sulfate in the absence of DTT (A) and the presence of DTT (B).

the other hand, the silica nanogelling did not hinder the siRNA release under the reductive environment with DTT (Fig. 4B), confirming that the reductive environment-sensitivity of the PCPs was maintained after the silica nanogelling. Thus, the silica nanogelling demonstrated to suppress the polyplex dissociation synergistically with disulfide cross-links in the polyplex core under the non-reductive condition, while the disulfide cleavage under the reductive condition could lead to the siRNA release from the SPCPs. The mechanism for the reductive environment-sensitivity of SPCPs might be explained by the effect of PEG palisade interfering with silica nanogelling, as follows. In reductive environments, the reducing molecules can reach the polyplex core through pore channels of the silica gel layer, inducing the core disulfide cleavage. This event can render the polyplex core unstable and also the adjacent PEG chains more fluidic, possibly destabilizing the silica gel layer toward the release of enclosed siRNA.

3.5. Time-dependent gene silencing assay

Gene silencing activity of PCP and SPCP-30 was monitored over time in cultured HeLa-Luc cells using AB-2550 Kronos Dio instrument. In this assay, luciferase-based luminescence emitted from HeLa-Luc cells incubated with luciferin (luciferase substrate) was measured as an index for gene silencing activity, and thus siGL3 was used as a target sequence to inhibit luciferase expression, with siSCR as a control. Interestingly, SPCP-30 induced gradual decrease in the relative luciferase expression over 72 h, whereas the decrease observed for PCP leveled off at around 36 h (Fig. 5A). In particular, the significantly enhanced gene silencing activity of SPCP-30, compared to PCP, was obtained from 24 h ($P < 0.05$ at 24 h), and eventually reached twice as high as that of PCP (~29% for SPCP-30 *vs.* ~14% for PCP, $P < 0.05$ at 72 h). Note that significant gene silencing activity was not observed for SPCP-30 carrying siSCR, indicating the sequence-specific gene silencing activity of SPCP-30 carrying siGL3.

Next, the cytotoxicity of SPCP-30 was examined in the same cultured cells using the CCK-8 assay in order to ensure that the enhanced gene silencing activity of SPCP-30 was not associated with an adverse side effect on the cell metabolism or viability. Fig. 5B reveals that almost no cytotoxicity was observed for SPCP-30 carrying siSCR at the tested concentrations of siRNA (100–500 nM). Therefore, the SPCP formulation was demonstrated to enhance the gene silencing activity of PCPs without associated cytotoxicity.

3.6. Cellular uptake studies by flow cytometry

To elucidate the mechanism for the significantly improved gene silencing activity of SPCP-30 compared to PCP, in HeLa-Luc cells (Fig. 5A), the cellular internalization efficiency was compared between the two formulations. In some cases, enhanced transfection efficiency is correlated to enhanced cellular uptake of siRNA through endocytosis as the first event in the cellular delivery process. Thus, the uptake amount of siRNA delivered by PCP and SPCP-30 was quantitatively analyzed by a flow cytometry using Cy5-siRNA. While the cellular uptake of Cy5-siRNA in PCP was more efficient (~3 times higher fluorescence from cells, $p < 0.05$) than that in SPCP-30 at 3 h, longer incubation for 12 and 24 h resulted in

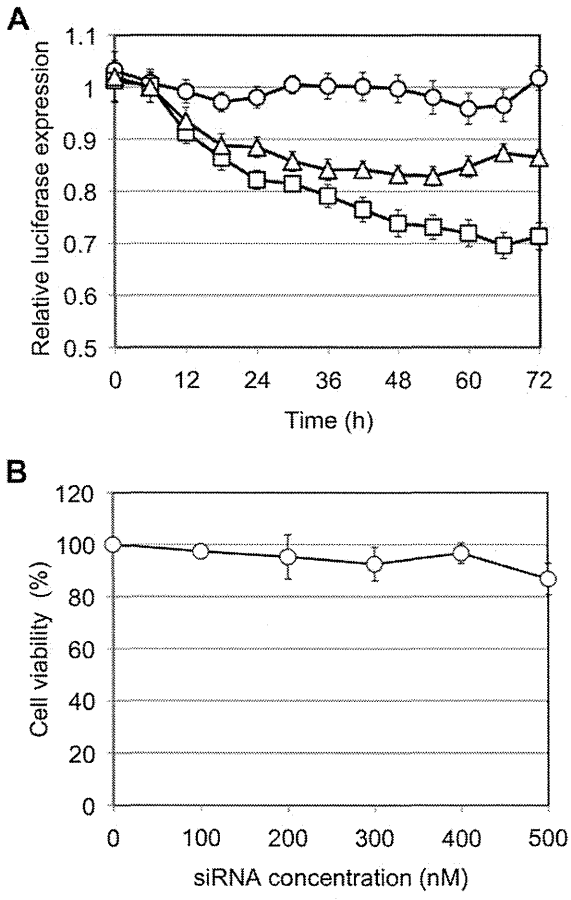

Fig. 5. (A) Time-dependent gene silencing activity of SPCP-30 with siGL3 (open square) in comparison with SPCP-30 with siSCR (open circle) and PCP with siGL3 (open triangle) in cultured HeLa-Luc cells (100 nM siRNA). The luminescence intensity in the cells treated with each polyplex was normalized to that in non-treated cells. Results are expressed mean and standard error of the mean ($n = 4$). (B) Viability of cultured HeLa-Luc cells treated with SPCP-30 carrying siSCR at varying concentrations for 24 h. Results are expressed as mean and standard error of the mean ($n = 8$).

similar uptake of Cy5-siRNA between PCP and SPCP-30 (Fig. 6). Thus, the enhanced gene silencing activity of SPCP-30, which was observed over 3 days, cannot be explained by discrepancies in the amount of siRNA internalized into cells.

3.7. Intracellular trafficking studies by CLSM observation

The enhanced gene silencing activity observed for the SPCP-30 formulation cannot be explained by a difference in cellular uptake, and thus, the mechanism of enhanced activity was further investigated on the subcellular level. Indeed, the endosomal entrapment of polyplexes following the endocytosis was investigated as another critical step in siRNA delivery, as it is believed that the bypass or the escape from the endosomal entrapment (and subsequent lysosomal degradation of siRNA) should be essential for successful RNAi in the cell cytoplasm [31]. Thus, the colocalization of siRNA with the late endosome/lysosome was observed by CLSM imaging using Cy5-siRNA (shown in red). In this experiment, late endosome/lysosome and the cell nuclei in HeLa-Luc cells were stained with LysoTracker Geen (shown in green) and Hoechst 33342 (shown in blue), respectively. After 24 h incubation, the cumulative amount of intracellular Cy5-siRNA was apparently similar between PCP and SPCP-30 (Fig. 7A and B), consistent with the result in the flow cytometric analysis (Fig. 6). Then, colocalization (%) of Cy5-siRNA with the late endosomes/lysosomes was calculated by dividing the colocalized Cy5 signal (yellow) with the total Cy5 signal (yellow and red). This analysis showed that approximately 40% of Cy5-siRNA in SPCP-30 was entrapped in the late endosome/lysosome, which was significantly lower than that in PCP ($\sim$68%, $p < 0.01$). This result indicates that SPCP-30-mediated siRNA delivery more efficiently evades the endosomal/lysosomal entrapment, compared to PCP, presumably leading to successful translocation to the cytoplasm toward the enhanced gene silencing activity (Fig. 5A).

Two possible explanations for the lower colocalization rate (or less endosomal entrapment) of SPCP-30 are; i) enhanced endosomal escaping functionality, and ii) modulation of the endocytic pathway toward bypass of the endosomal entrapment. With regard to the endosomal escaping functionality, it has been suggested that deprotonated silanol groups contained in silica, as reflected in the significantly negative ζ-potential of SPCPs (Table 1), can act as a proton acceptor in the acidic late endosome/lysosome (pH < 5.5), possibly facilitating the influx of chloride ions with protons and

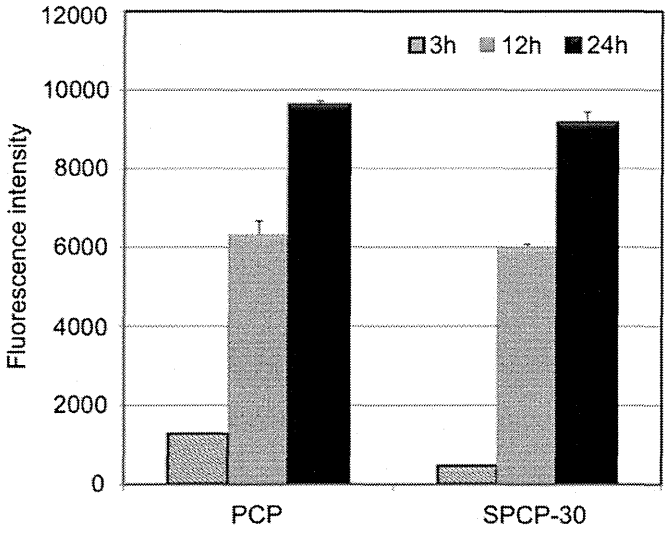

Fig. 6. Cellular uptake of Cy5-siRNA delivered by PCP and SPCP-30 in HeLa-Luc cells (300 nM Cy5-siRNA). Results are expressed as mean and standard error of the mean ($n = 3$).

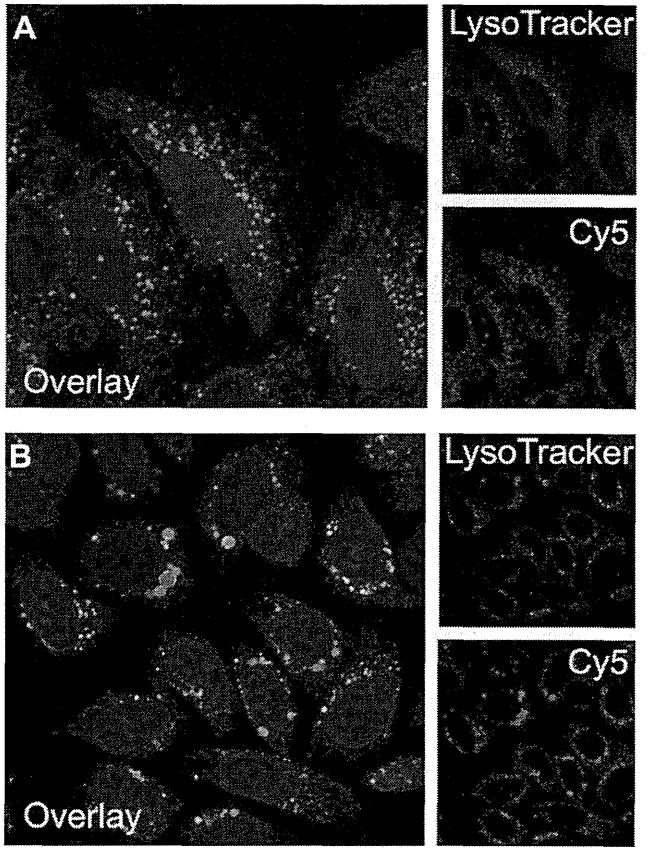

Fig. 7. Intracellular distribution of Cy5-siRNA delivered by PCP (A) and SPCP-30 (B) in HeLa-Luc cells stained with LysoTracker Green and Hoechst 33342 for the late endosome/lysosome and the nuclei, respectively.

increasing the osmotic pressure in the vesicles for the membrane disruption (the proton sponge hypothesis) [31,41,42]. On the other hand, endocytic pathways are also known to affect the intracellular trafficking of endocytosed macromolecules. Among endocytic pathways, macropinocytosis is known as a large-scale fluid endocytic pathway, where the protrusions of highly ruffled invaginations of the plasma membrane extend to engulf a large volume of the surrounding extracellular fluid upon fusing back with themselves or with the plasma membrane to form intracellular uncoated vacuoles, termed macropinosome, with a size of 0.5–10 μm [43]. Interestingly, macropinosomes are reported to be more leaky vesicles compared to the other types of endocytic vesicles, and further not to be necessarily fused with the lysosome [44,45], thereby considered as a potential pathway for enhanced nucleic acid delivery. In addition, several previous studies have reported that silica nanoparticles are significantly uptaken by cells through the macropinocytosis, although other endocytic pathways also contribute to their cellular uptake [46,47].

Accordingly, to elucidate whether SPCP-30 can enter the cells through macropinocytosis, an inhibition assay was performed for HeLa-Luc cells incubated with amiloride, a specific inhibitor of macropinocytosis *via* inhibition of Na^+/H^+ exchange proteins [48]. Considering the fact that cells uptake essential nutrients from external media through endocytic pathways, including macropinocytosis, the inhibition of endocytic pathways might lead to the perturbation of cell homeostasis or ultimately the cell death [49]. A preliminary study suggested that 3 h incubation of the cells with 1.5 mM amiloride should be suitable for minimizing the decrease in the cell viability (data not shown). Treatment of the cells with amiloride significantly decreased the mean fluorescence intensity

from Cy5-siRNA for both PCP and SPCP-30, *i.e.*, the decreasing rate was ~20% for PCP and ~50% for SPCP-30 ($p < 0.05$) in the flow cytometric analysis, indicating that both polyplexes can undergo the macropinocytosis for the cell entry. Nevertheless, the stronger inhibitory effect in SPCP-30 indicates that the silica nanogelling increases a portion of macropinocytosed polyplexes, and also that one of the major endocytic pathways for SPCP-30 is the macropinocytosis. Hence, the assumption that SPCP-30 can evade the endosomal entrapment through the modulated endocytic pathway was consistent with the experimental results.

4. Conclusions

In the present study, the silica nanogelling of PCPs carrying siRNA through silicate condensation was developed for enhanced siRNA carrier stability and functionality. The simple mixing of the platform PCPs with silicates (>10 mM) resulted in successful preparation of silica nanogel-coated PCPs, *i.e.*, the SPCP formulation, featuring a hydrodynamic size of approximately 140 nm with a relatively narrow size distribution (PdI < 0.2) and a negative ζ-potential (~−15 mV), which was in sharp contrast with the positive platform PCPs (~+10 mV) (Table 1). Furthermore, the STEM-EDX analysis directly confirmed the presence of silica on the SPCP surface (Fig. 3). The silica nanogelling substantially suppressed the polyplex dissociation (or siRNA release) induced by the counter polyanion exchange under the non-reductive condition, while allowing the siRNA release under the reductive condition produced with DTT, indicating the reversible stability of SPCPs (Fig. 4). SPCP prepared at 30 mM silicate (SPCP-30) improved the sequence-specific gene silencing activity compared to the platform PCP (Fig. 5A) and also maintained the cell viability (>85%) even at the high concentration tested (500 nM siRNA) against HeLa-Luc cells (Fig. 5B). The enhanced gene silencing of SPCP-30 was apparently correlated with the less endosomal entrapment of the delivered siRNA (Fig. 7), which could be so far explained by two mechanisms; one is the enhanced endosomal escape induced by the proton sponge hypothesis based on deprotonated silanol groups contained in silica, and the other is the modulation in the endocytic pathways, *e.g.*, macropinocytosis, possibly evading the lysosomal degradation of siRNA. In conclusion, this work demonstrates a promising approach to enhance stability and functionality of siRNA-incorporating polyplexes for successful siRNA delivery.

Acknowledgment

This research was financially supported by the Funding Program for World-Leading Innovative R&D on Science and Technology (FIRST) from the Japan Society for the Promotion of Science (JSPS), and also by Izumi Science and Technology Foundation. A part of this work was conducted in Research Hub for Advanced Nano Characterization, The University of Tokyo, supported by the Ministry of Education, Culture, Sports, Science and Technology (MEXT), Japan. N. Gouda acknowledges the fellowship from Ministry of Education, Science, Sports and Culture (MEXT), Japan. We are grateful to Mr. H. Hoshi (JEOL Ltd.) for his technical support.

Appendix A. Supplementary data

Supplementary data related to this article can be found at http://dx.doi.org/10.1016/j.biomaterials.2012.09.077.

References

[1] Elbashir SM, Harborth J, Lendeckel W, Yalcin A, Weber K, Tushl T. Duplexes of 21-nucleotide RNAs mediate interference in cultured mammalian cells. Nature 2001;411(6836):494–8.
[2] de Fougerolles A, Vornlocher HP, Maraganore J, Lieberman J. Interfering with diseases: a progress report on siRNA-based therapeutics. Nat Rev Drug Discov 2007;6(6):443–53.
[3] Burnett JC, Rossi JJ. RNA-based therapeutics: current progress and future prospects. Chem Biol Rev 2012;19(1):60–71.
[4] Fire A, Xu S, Montgomery MK, Kostas SA, Driver SE, Mello CC. Potent and specific genetic interference by double-stranded RNA in *Caenorhabditis elegans*. Nature 1998;391(6669):806–11.
[5] Zimmermann TS, Lee ACH, Akinc A, Bramlage B, Bumcrot D, Fedoruk MN, et al. RNAi-mediated gene silencing in non-human primates. Nature 2006; 441(7089):111–4.
[6] Nakamura Y, Kogure K, Futaki S, Harashima H. Octaarginine-modified multifunctional envelope-type nano device for siRNA. J Control Release 2007; 119(3):360–7.
[7] Akinc A, Zumbuehl A, Goldberg M, Leshchiner ES, Busini V, Hossain N, et al. A combinatorial library of lipid-like materials for delivery RNAi therapeutics. Nat Biotechnol 2008;26(5):561–9.
[8] Semple SC, Akinc A, Chen J, Sandhu AP, Mui BL, Cho CK, et al. Rational design of cationic lipids for siRNA delivery. Nat Biotech 2010;28(2):172–6.
[9] Itaka K, Kanayama N, Nishiyama N, Jang WD, Yamasaki Y, Nakamura K, et al. Supramolecular nanocarrier of siRNA from PEG-based block catiomer carrying diamine side chain with distinctive pKa directed to enhance intracellular gene silencing. J Am Chem Soc 2004;126(42):13612–3.
[10] Kumar P, Wu H, McBride JL, Jung KE, Kim MH, Davidson BL, et al. Transvascular delivery of small interfering RNA to the central nervous system. Nature 2007;448(7149):39–45.
[11] Meyer M, Philipp A, Oskuee R, Schmidt C, Wagner E. Breathing life into polycations: functionalization with pH-responsive endosomolytic peptides and polyethylene glycol enables siRNA delivery. J Am Chem Soc 2008;130(11): 3272–3.
[12] Davis ME, Zuckerman JE, Choi CHJ, Seligson D, Tolcher A, Alabi CA, et al. Evidence of RNAi in humans from systemically administered siRNA via targeted nanoparticles. Nature 2010;464(7291):1067–70.
[13] Shimizu H, Hori Y, Kaname S, Yamada K, Nishiyama N, Matsumoto S, et al. siRNA-based therapy ameliorates glomerulonephritis. J Am Soc Nephrol 2010; 21(4):622–33.
[14] Kim HJ, Ishii A, Miyata K, Lee Y, Wu S, Oba M, et al. Introduction of stearoyl moieties into a biocompatible cationic polyaspartamide derivative, PAsp(-DET), with endosomal escaping function for enhanced siRNA-mediated gene knockdown. J Control Release 2010;145(2):141–8.
[15] Schaffert D, Troiber C, Salcher EE, Frohlich T, Martin I, Badgujar N, et al. Solid-phase synthesis of sequence-defined T-, i-, and U-shape polymers for pDNA and siRNA delivery. Angew Chem Int Ed 2011;50(38):8986–9.
[16] Siegwart DJ, Whitehead KA, Nuhn L, Sahay G, Cheng H, Jiang S, et al. Combinatorial synthesis of chemically diverse core-shell nanoparticles for intracellular delivery. Proc Natl Acad Sci U S A 2011;108(32):12996–3001.
[17] Suma T, Miyata K, Ishii T, Uchida S, Uchida H, Itaka K, et al. Enhanced stability and gene silencing ability of siRNA-loaded polyion complexes formulated from polyaspartamide derivatives with a repetitive array of amino groups in the side chain. Biomaterials 2012;33(9):2770–9.
[18] Giljohann DA, Seferos DS, Prigodich AE, Patel PC, Mirkin CA. Gene regulation with polyvalent siRNA-nanoparticle conjugates. J Am Chem Soc 2009;131(6): 2072–3.
[19] Singh N, Agrawal A, Leung AKL, Sharp PA, Bhatia SN. Effect of nanoparticle conjugation on gene silencing by RNA interference. J Am Chem Soc 2010; 132(24):8241–3.
[20] Zheng D, Giljohann DA, Chen DL, Massich MD, Wang XQ, Iordanov H, et al. Topical delivery of siRNA-based spherical nucleic acid nanoparticle conjugates for gene delivery. Proc Natl Acad Sci U S A 2012;109(30):11975–80.
[21] Kakizawa Y, Furukawa S, Kataoka K. Block copolymer-coated calcium phosphate nanoparticles sensing intracellular environment for oligodeoxynucleotide and siRNA delivery. J Control Release 2004;97(2):345–56.
[22] Xia TA, Kovochich M, Liong M, Meng H, Kabehie S, SGeorge S, et al. Polyethyleneimine coating enhances the cellular uptake of mesoporous silica nanoparticles and allows safe delivery of siRNA and DNA constructs. ACS Nano 2009;3(10):3273–86.
[23] Pittella F, Zhang M, Lee Y, Kim HJ, Tockary T, Osada K, et al. Enhanced endosomal escape of siRNA-incorporating hybrid nanoparticles from calcium phosphate and PEG-block charge-conversional polymer for efficient gene knockdown with negligible cytotoxicity. Biomaterials 2011;32(11): 3106–14.
[24] Lee MY, Park SJ, Park K, Kim KS, Lee H, Hahn SK. Targeted-specific gene silencing of layer-by-layer assembled gold-cysteamine/siRNA/PEI/HA nanocomplex. ACS Nano 2011;5(8):6138–47.
[25] Saito G, Swanson JA, Lee KD. Drug delivery strategy utilizing conjugation via reversible disulfide linkages: role and site of cellular reducing activities. Adv Drug Deliv Rev 2003;55(2):199–215.
[26] Kakizawa Y, Harada A, Kataoka K. Environment-sensitive stabilization of core-shell structured polyion complex micelle by reversible cross-linking of the core through disulfide bond. J Am Chem Soc 1999;121(48):11247–8.
[27] Matsumoto S, Christie RJ, Nishiyama N, Miyata K, Ishii A, Oba M, et al. Environment-responsive block copolymer micelles with a disulfide cross-linked core for enhanced siRNA delivery. Biomacromolecules 2009;10(1):119–27.
[28] Christie RJ, Miyata K, Matsumoto Y, Nomoto T, Menasco D, Lai TC, et al. Effect of polymer structure on micelles formed between siRNA and cationic block

copolymer comprising thiols and amidines. Biomacromolecules 2011;12(9):3174–85.
[29] Christie RJ, Matsumoto Y, Miyata K, Nomoto T, Fukushima S, Osada K, et al. Targeted polymeric micelles for siRNA treatment of experimental cancer by intravenous injection. ACS Nano 2012;6(6):5174–89.
[30] Kakizawa Y, Kataoka K. Block copolymer micelles for delivery of gene and related compounds. Adv Drug Deliv Rev 2002;54(2):203–22.
[31] Miyata K, Nishiyama N, Kataoka K. Rational design of smart supramolecular assemblies for gene delivery: chemical challenges in the creation of artificial viruses. Chem Soc Rev 2012;41(7):2562–74.
[32] Nomoto T, Matsumoto Y, Miyata K, Oba M, Fukushima S, Nishiyama N, et al. In situ quantitative monitoring of polyplexes and polyplex micelles in the blood circulation using intravital real-time confocal laser scanning microscopy. J Control Release 2011;151(2):104–9.
[33] Mizutani T, Nagase H, Ogoshi H. Silicic acid polymerization catalyzed by amines and polyamines. Chem Lett 1998:133–4.
[34] Coradin T, Durupthy O, Livage J. Interactions of amino-containing peptides with sodium silicate and colloidal silica: a biomimetic approach of silicification. Langmuir 2002;18(6):2331–6.
[35] Miyata K, Gouda N, Takemoto H, Oba M, Lee Y, Koyama H, et al. Enhanced transfection with silica-coated polyplexes loading plasmid DNA. Biomaterials 2010;31(17):4764–70.
[36] Suma T, Miyata K, Anraku Y, Watanabe S, Christie RJ, Takemoto H, et al. A smart multilayered assembly for biocompatible siRNA delivery featuring dissolvable silica. Endosome-disrupting Polycation. Detachable PEG ACS Nano 2012;6(8):6693–705.
[37] Fleming BA. Kinetics of reaction between silicic acid and amorphous silica surfaces in NaCl solutions. J Colloid Interface Sci 1986;110(1):40–64.
[38] Popplewell JF, King SJ, Day JP, Ackrill P, Fifield LK, Cresswell RG, et al. Kinetics of uptake and elimination of silicic acid by a human subject: a novel application of ^{32}Si and accelerator mass spectromerty. J Inorg Biochem 1998;69(3):177–80.
[39] Harada A, Kataoka K. Formation of polyion complex micelles in an aqueous milieu from a pair of oppositely-charged block copolymers with poly(ethylene glycol) segments. Macromolecules 1995;28(15):5294–9.
[40] Kobayashi M, Juillerat F, Calletto P, Bowen P, Borkovec M. Aggregation and charging of colloidal silica particles: effect of particle size. Langmuir 2005;21(13):5761–9.
[41] Boussif O, Lezoualc'h F, Zanta MA, Mergny MD, Scherman D, Demeneix B, et al. A versatile vector for gene and oligonucleotide transfer into cells in culture and in-vivo. Proc Natl Acad Sci U S A 1995;92(16):7297–301.
[42] Slowing I, Vivero-Escoto JL, Wu CW, Lin VSY. Mesoporous silica nanoparticles as controlled release drug delivery and gene transfection carrier. Adv Drug Deliv Rev 2008;60(11):1278–88.
[43] Mercer J, Helenius A. Virus entry by macropinocytosis. Nat Cell Biol 2009;11(5):510–20.
[44] Wadia JS, Stan RV, Dowdy SF. Transducible TAT-HA fusogenic peptide enhances escape of TAT-fusion proteins after lipid raft macropinocytosis. Nat Med 2004;10(3):310–5.
[45] Khalil IA, Kogure K, Futaki S, Harashima H. High density of octaarginine stimulates macropinocytosis leading to efficient intracellular trafficking for gene expression. J Biol Chem 2006;281(6):3544–51.
[46] Zhang YY, Hu L, Yu DH, Gao CY. Influence of silica particle internalization on adhesion and migration of human dermal fibroblasts. Biomaterials 2010;31(32):8465–74.
[47] Meng H, Yang S, Li ZX, Xia T, Chen J, Ji ZX, et al. Aspect ratio determines the quantity of mesoporous silica nanoparticle uptake by a small GTPase-dependent macropinocytosis mechanism. ACS Nano 2011;5(6):4434–47.
[48] Hewlett L, Prescott A, Watts C. The coated pit and macropinocytic pathways serve distinct endosome populations. J Cell Biol 1994;124(5):689–703.
[49] von Gersdorff K, Sanders NN, Vandenbroucke R, De Smedt SC, Wagner E, Ogris M. The internalization route resulting in successful gene expression depends on both cell line and polyethylenimine polyplex type. Mol Ther 2006;14(5):745–53.

JOC The Journal of Organic Chemistry

Article

pubs.acs.org/joc

Solid-Phase Synthesis of *P*-Boronated Oligonucleotides by the *H*-Boranophosphonate Method

Sho Uehara,[†] Shingo Hiura,[†] Renpei Higashida,[†] Natsuhisa Oka,[‡] and Takeshi Wada*[,†,§]

[†]Department of Medical Genome Sciences, Graduate School of Frontier Sciences, The University of Tokyo, Bioscience Building 702, 5-1-5 Kashiwanoha, Kashiwa, Chiba 277-8562, Japan,

[‡]Department of Chemistry and Biomolecular Science, Faculty of Engineering, Gifu University, 1-1 Yanagido, Gifu 501-1193, Japan,

[§]Department of Medicinal and Life Science, Faculty of Pharmaceutical Sciences, Tokyo University of Science, 2641 Yamazaki, Noda, Chiba 278-8510, Japan

Supporting Information

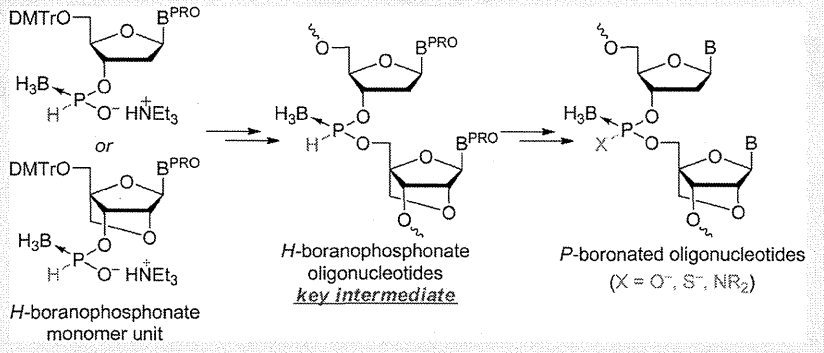

ABSTRACT: Recently, *P*-boronated oligonucleotides have been attracting much attention as potential therapeutic oligonucleotides. In this study, we developed *H*-boranophosphonate oligonucleotide bearing a borano group and hydrogen atom on the internucleotidic phosphorus and demonstrated that this novel *P*-boronated oligonucleotide is a versatile precursor to various *P*-boronated oligonucleotides such as boranophosphate, boranophosphorothioate, and boranophosphoramidate. The method was also applicable to the synthesis of a locked nucleic acid-modified boranophosphate oligonucleotide, which exhibited a dramatically enhanced affinity to complementary oligonucleotides.

INTRODUCTION

Chemical modifications of the internucleotidic phosphate linkages of oligonucleotides have been widely used for the stabilization of unmodified natural oligonucleotides, which are inherently labile to nucleases, especially for therapeutic purposes.[1] Such modifications have also been used to improve their cellular uptake for the same purposes.[2] Phosphorothioate oligonucleotides (PS-ODNs) modified with sulfur have been particularly studied:[3] two therapeutic oligonucleotides have been approved, and many of them are in clinical trials.[4] However, they suffer from some drawbacks such as nonspecific binding to proteins and toxicity, which has brought forth the need for novel P-modified oligonucleotides that are more suitable for therapeutic use.[3]

Recently, P-boronated oligonucleotides have attracted much attention as potential therapeutic oligonucleotides because lower toxicity than that of their phosphorothioate counterparts is expected.[5] Moreover, their stability to nucleases is even higher than that of PS-ODNs, and high potency for gene suppression has been demonstrated.[5b,6] Furthermore, they are also potential ^{10}B carriers for boron neutron capture therapy for cancer treatment;[6] however, synthetically available P-boronated oligonucleotides are still very limited, despite intensive efforts by many researchers.[7−10] To find potent therapeutic oligonucleotides, the diversity of P-boronated oligonucleotides that are synthetically available needs to be expanded.

The methods for the synthesis of P-boronated oligonucleotides to date have generally been developed on an individual basis; synthesizing different kinds of P-boronated oligonucleotides requires different methods and different sets of monomer units.[7−10] In this study, rather than following the conventional strategies, we developed a novel type of P-boronated oligonucleotide, H-boranophosphonate oligonucleotide, with the expectation that it could be used as a versatile precursor to various P-boronated oligonucleotides via substitutions of the hydrogen atoms of its H−P→BH_3 backbone (Scheme 1). A similar strategy has been used for the synthesis of P-modified oligonucleotides using H-phosphonate precursors.[11] In fact, the diversity of P-modified oligonucleotides has been greatly expanded since the development of H-phosphonate oligonucleotides. Although H-boranophosphonate diesters cannot be

Received: January 24, 2014
Published: March 28, 2014

Scheme 1. Synthesis of Diverse *P*-Boronated Oligonucleotides Using *H*-Boranophosphonate Oligonucleotides As Platforms[a]

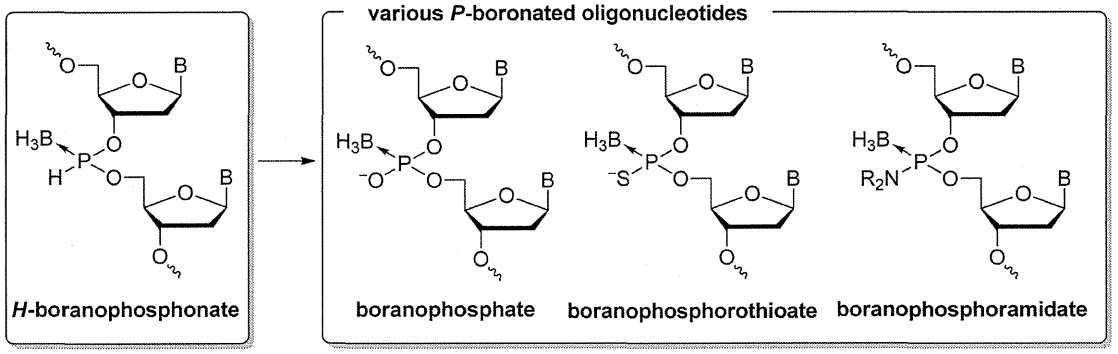

[a]B = Nucleobase.

Table 1. Synthesis of 3′-*H*-Boranophosphonate Monomers 3a–e[a]

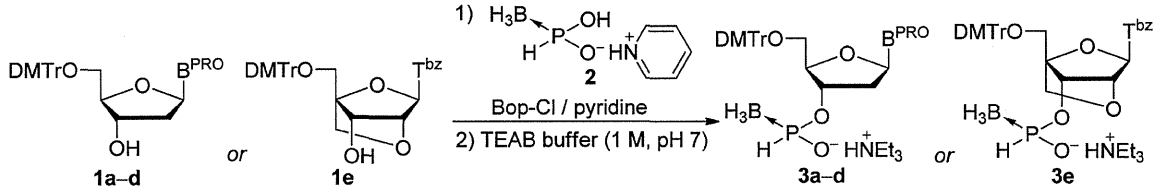

entry	1 (B^{PRO})	reagents and conditions	yield of 3 [%]
1	a (T^{bz})	2 (1.2 equiv), Bop-Cl (1.2 equiv) rt, 1 h	95
2	b (A^{bz})	2 (2.0 equiv), Bop-Cl (2.0 equiv), 0 °C to rt, 25 min	72
3	c (C^{ibu})	2 (2.0 equiv), Bop-Cl (2.0 equiv), 0 °C to rt, 30 min	60
4	d ($G^{ce,ibu}$)	2 (2.0 equiv), Bop-Cl (2.0 equiv), 0 °C to rt, 15 min	74
5	e (T^{bz})	2 (2.0 equiv), Bop-Cl (2.0 equiv), 0 °C to rt, 20 min	75

[a]B^{PRO} = Protected nucleobase; T^{bz} = N^3-benzoylthymin-1-yl; A^{bz} = N^6-benzoyladenin-9-yl; C^{ibu} = N^4-isobutyrylcytosin-1-yl; $G^{ce,ibu}$ = O^6-cyanoethyl-N^2-isobutyrylguanin-9-yl; Bop-Cl = bis(2-oxo-3-oxazolidinyl)phosphinic chloride; TEAB = triethylammonium bicarbonate; DMTr = 4,4′-dimethoxytrityl.

derivatized via tautomerization to the tricoordinate forms, as in the case of their H-phosphonate counterparts, it has been demonstrated independently by Montchamp et al.[12] and our group[13] that the P–H function of H-boranophosphonate diesters can be modified by deprotonation and subsequent reactions with electrophiles. The chemistry of secondary phosphine–borane complexes and their analogues[14] was also used for the development of our novel strategy.

RESULTS AND DISCUSSION

Synthesis of 3′-*H*-Boranophosphonate Monomers 3a–e. Table 1 summarizes the synthesis of the 2′-deoxyribonucleoside 3′-*H*-boranophosphonate monomers **3a–d** and locked nucleic acid (LNA)[15] thymidine 3′-*H*-boranophosphonate monomer **3e**. 2′-Deoxythymidine monomer **3a** was obtained in 95% from the thymidine derivative bearing the 3′-OH **1a** and pyridinium *H*-boranophosphonate **2** according to the procedure described in the literature.[13a] 2′-Deoxyadenosine, cytosine, guanosine, and LNA thymidine monomers **3b–e** were synthesized by the method for the synthesis of **3a** with some modifications.

Solid-Phase Synthesis of *PBX*-ODNs. Scheme 2 shows the synthesis of *P*-boronated oligodeoxyribonucleotides bearing oxygen, sulfur,[16,17] or 2-morpholinoethylamino[18] as the substituent X on the phosphorus atoms (*PBX*-ODNs) *via* *H*-boranophosphonate oligodeoxyribonucleotides (*PBH*-ODNs). The monomers **3a–e** were condensed with the 5′-OH of nucleosides or oligonucleotides on a controlled-pore glass (CPG) in the presence of 1,3-dimethyl-2-(3-nitro-1,2,4-triazol-1-yl)-2-pyrrolidin-1-yl-1,3,2-diazaphospholidinium hexafluorophosphate (MNTP)[19] and 2,6-lutidine, and the 5′-end was deprotected by 3% dichloroacetic acid (DCA). Released dimethoxytrityl (DMTr) cations were reduced by Et_3SiH, because they would otherwise cause side reactions with the internucleotidic BH_3 groups.[20] The *PBH*-ODN chains were elongated by this cycle, and the modification of the phosphorus atoms and subsequent deprotection afforded *PBX*-ODNs.

First, *PBX*-ODN 2mers were synthesized using this cycle to optimize reaction conditions for the synthesis of oligomers. The monomers **3a–d** were condensed with the 5′-OH of N^3-benzoylthymidine anchored to a CPG *via* a succinate linker using MNTP and 2,6-lutidine to afford the *PBH*-ODN 2mers on a solid support (Scheme 2, **5**, n = 0). Subsequently, 5′-detritylation, *P*-modification (oxidation, sulfurization, or amination), deprotection, and cleavage of the linker afforded the desired *PBX*-ODN 2mers. *P*-Oxidation of the *PBH*-ODN 2mers on a solid support was performed *via* oxidative *P*-chlorination with CCl_4 and subsequent nucleophilic substitution by H_2O in the presence of *i*-Pr_2NEt (Scheme 3, oxidation).[21] *N*,*N*′-Dimethylthiuram disulfide (DTD)[22] and *i*-Pr_2NEt were used for the *P*-sulfurization step (Scheme 3, sulfurization). The introduction of a 2-morpholinoethylamino group onto the phosphorus atom was performed *via* oxidative *P*-chlorination with CCl_4 and subsequent reaction with 4-(2-

dx.doi.org/10.1021/jo500185b | J. Org. Chem. 2014, 79, 3465–3472